

# Atomistic investigation of dislocation-assisted carbon migration in iron

Tigany Zarrouk

July 15, 2021

## Contents

<b>1</b>	<b>Introduction</b>	<b>4</b>
<b>2</b>	<b>Computational Method</b>	<b>5</b>
2.1	Peierls Potential . . . . .	6
2.2	Preliminary calculations . . . . .	6
2.3	Fe-C binding energies . . . . .	9
2.4	Carbon concentration on dislocation line . . . . .	9
2.5	Line Tension Model . . . . .	10
2.5.1	Line-tension model in carbon environment . . . . .	11
2.5.2	Extension to more Fermi-Dirac statistics . . . . .	11
<b>3</b>	<b>Results</b>	<b>12</b>
3.1	Peierls Potential . . . . .	12
3.2	Preliminary calculations . . . . .	15
3.3	Fe-C binding energies . . . . .	16
3.4	Carbon concentration along on line . . . . .	20
3.5	Line Tension Model . . . . .	22
3.5.1	Prerequisites . . . . .	22
3.5.2	Kink-pair formation in pure iron . . . . .	22
3.5.3	Kink-pair formation enthalpy with a single carbon . . . . .	25
3.5.4	Kink-pair nucleation rate . . . . .	28
3.5.5	Kink-trapping . . . . .	30
3.6	Line-tension equilibrium conditions . . . . .	30
3.6.1	Dynamics of straight $1/2\langle 111 \rangle$ screw dislocation . . . . .	30
3.6.2	Dynamics of kink-pair formation in equilibrium . . . . .	30
3.7	Diffusion Barriers . . . . .	34
3.7.1	Theory . . . . .	35
3.7.2	Computational Method . . . . .	35
3.7.3	Enthalpies in dislocation movement with static carbon . . . . .	36
3.7.4	Modification of occupancies due to diffusion barrier . . . . .	37
<b>4</b>	<b>Discussion</b>	<b>38</b>
<b>5</b>	<b>Future work</b>	<b>39</b>
<b>6</b>	<b>Conclusion</b>	<b>40</b>

<b>7</b>	<b>Appendix</b>	<b>41</b>
7.1	Regularisation of interaction energy in quadrupolar array . . . . .	41
7.2	Zero-point energy calculation . . . . .	41
7.3	Smooth mapping of sites in equilibrium line-tension model . . . . .	42
<b>8</b>	<b>Bibliography</b>	<b>42</b>

## Abstract

Martensitic bearing steels have been shown to undergo subsurface microstructural decay, forming Dark Etching Regions (DERs), promoting failure through rolling contact fatigue (RCF). Dislocation-assisted carbon migration is thought to be the underlying mechanism, yet empirical studies have been inconclusive as to how dislocations move carbon and where excess carbon from the martensitic matrix migrates to upon transformation to ferrite—a phase of significantly lower carbon solubility. In this report, we detail the first stages of a multi-scale modelling approach to elucidate carbon transport by dislocations. Tight-binding simulations of carbon interactions with the  $1/2\langle 111 \rangle$  screw dislocation found solute distribution to vary significantly within  $\sim 2b$  of the easy and hard cores; the highest binding energy being found in the centre of the hard screw core—which is the ground state carbon-dislocation configuration—in agreement with Density Functional Theory (DFT). Determination of equilibrium carbon concentration along dislocation lines, at various dislocation densities and nominal carbon concentrations, found most sites around the hard core were saturated, with all easy cores reconstructing to hard due to saturation of adjacent octahedral sites. In the typical temperature range of bearing operation, we expect all dislocations to be of hard core type, pinned by carbon in a prismatic site within the dislocation core. We anticipate large drag forces acting on dislocations in the initial stages of glide, due to carbon-dislocation binding. Line-tension modelling of kink-pair formation shows a small, but consistent, reduction in the kink-pair formation enthalpy with carbon ahead of the dislocation, for all stresses, resulting in a modest increase in average dislocation velocity. In conditions allowing for carbon to equilibrate between trap sites, the average kink-pair formation enthalpy is reduced, increasing dislocation velocity, however a self-consistent method is necessary for accurate results, which is left for future work. For a solute-drag mechanism of dislocation-assisted carbon migration, the reduction in migration energy between carbon sites in the vicinity of a screw dislocation is crucial for its potential validity, such that carbon can keep up with dislocations upon movement. Measurement of these migration barriers using a quantum-mechanical method will provide us with more accurate predicted stress and temperature regimes in which solute drag by screw dislocations is a valid mechanism. These results provide data for the last stage in this multi-scale approach: self-consistent kinetic Monte Carlo (SCKMC) simulations incorporating solute diffusion, to ascertain how carbon moves with dislocations in different stress, temperature and concentration regimes.

# 1 Introduction

Martensitic steels are frequently used in bearings due to their resilience to service conditions, being subject to high rotational speeds and contact pressures. However, under cyclic loading exceeding a given contact stress, the microstructure of the steel can decay due to the accumulation of plasticity. This signals the onset of rolling contact fatigue (RCF), which increases the risk of failure from subsurface crack initiation. The microstructural decay corresponds to the observation of Dark Etching Regions (DERs) as seen in optical microscopy, where the darkness of these regions is due to the higher reactivity of DER phases to the etchant; exacerbated by the roughness of the DER region [1]. See figure 1.

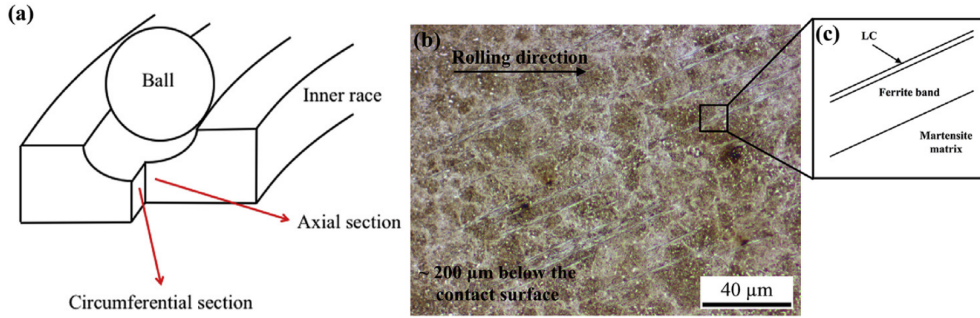


Figure 1: Diagram of DER location within a bearing and its characteristics, taken from [2]. (a) Axial and circumferential sections of a bearing inner ring. (b) Circumferential section of a bearing inner ring under optical microscope, where ferrite bands (white etching bands) are formed in the subsurface. (c) Diagram showing the structure of a WEB consisting of a ferrite band and a LC adjacent to it. One can see the DER region is composed of regions of ferrite interspersed in the parent martensite with lenticular carbides bordering the ferrite bands.

Decay of the martensitic microstructure is complex, with observation of many different phenomena. Martensite transforms to ferrite microbands as a result of strain localization [2, 3, 4, 5, 6, 7, 8, 9, 10]. Residual carbides, untouched at the start of DER formation, gradually dissolve within ferrite and martensite [5, 6, 11]. Further RCF progression leads to the formation of low and high angle ferrite features, White Etching Bands (WEBs), composed of nanocrystalline [7, 11, 12] and elongated ferrite [10]. Lenticular carbides precipitate at the boundaries of these ferrite bands [6, 11]. Thickening of these carbides occurs during DER development and is correlated with WEB growth [2, 13, 14, 15]. Reductions in dislocation density in nanocrystalline (heavily deformed) ferrite have been observed in the later stages of DER formation [1, 16].

Carbon migration is thought to be the mechanism by which this degradation occurs, but it is not definitively known how or where carbon migrates with the onset of DER formation. The key questions are: where does excess carbon from the martensitic matrix find itself when the structure decays to low solubility (0.02 wt%) ferrite? and how is the carbon transported, given its low diffusivity in martensite/DER phases [17]?

Fu *et al.* propose that carbon atoms inside the martensite would segregate to pre-existing/residual carbides, increasing their size [13]. This theory was successfully applied to the growth of lenticular carbides [2], however, problems arise with the application to temper carbide growth: if carbides were to form in martensite, they should follow

the Bagaryatskii/Isaichev orientation relationship, but observations suggest a lack of any orientation relationship [18]. Temper carbides residing within DERs have irregular shapes/diffuse boundaries, which are seemingly due to the incomplete *dissolution* of *temper* carbides, which is at odds with the theory of Fu *et al.*.

A plausible mechanism for carbon migration is that it is driven by dislocation glide, which is as follows [2, 6, 8, 13, 14, 15]. Due to the high dislocation density exhibited in martensite, carbon segregates to dislocations in Cottrell atmospheres, causing pinning. Strain generated by cyclic stresses allow dislocations to escape their carbon rich environment. The free dislocations re-attract carbon, allowing the Cottrell atmospheres to reform, subsequently re-pinning the dislocations, creating a net carbon flux. This mechanism allows for the movement of carbon during the martensite-ferrite transition, while also explaining how excess carbon can move from the ferrite phases to lenticular carbides at the boundaries, describing the process behind both WEB growth and carbide thickening. Moreover, it explains the dissolution of residual carbides, both in ferrite WEBs and martensite, due to dislocation rearrangement and pile ups at the carbide interface drawing carbon atoms out, due to a more favourable binding to dislocations. However, as to how this process occurs on the atomistic scale, or if it is indeed feasible, is unknown.

Experimentally probing dislocation-assisted carbon migration has proven difficult and inconclusive. Work needs to be done to understand dislocation-carbon interactions; more specifically: how dislocations move carbon within the temperature and stress regimes experienced during operation; where carbon is transported to and what the resultant dislocation networks are.

To shed light on this mechanism, a multi-scale modelling approach can be used. Atomistics can provide information of the 2d Peierls energy landscape which dislocations are subject to in iron; and how this landscape is modified by the binding of carbon to dislocations. This data can be used in a line tension model of a dislocation to determine the kink-pair formation energies of dislocations as a function of carbon content and stress. Finally, one can use a kinetic Monte Carlo (kMC) model of dislocation glide by thermally activated kink-pair nucleation, in an environment of carbon. From this last stage of coarse-graining, one can determine in which regimes of temperature, stress and carbon concentration, dislocation-assisted carbon migration becomes a feasible mechanism behind DER formation, with predictions of dislocation velocity, dislocation configurations and where carbon moves with dislocation glide.

In this report, we will focus on the atomistic portion of this project, directed at understanding dislocation-carbon interactions at the atomistic scale in ferrite (bcc iron). With further knowledge of the fundamental mechanism behind DER formation, we can hope to suppress dislocation motion in the martensitic matrix, mitigating failure by RCF.

## 2 Computational Method

We use the tight-binding model of Paxton and Elsässer [19], which has been shown to describe the binding energies of carbon complexes in bcc iron, in good agreement with DFT calculations. This model reproduces the two screw dislocation core structures—the easy and hard  $1/2\langle 111 \rangle$  cores—exhibited in bcc iron. Study of both is crucial to understanding solute-dislocation interactions. The easy core is the ground state in pure iron, but solutes, such as hydrogen and carbon, have been shown to reconstruct this core into the hard core configuration [20, 21]. Computationally cheaper models, which do not

incorporate quantum mechanics, such as the EAM, cannot reproduce these behaviours.

## 2.1 Peierls Potential

To determine the Peierls potential of the  $1/2\langle 111 \rangle$  screw dislocation, we followed the procedure detailed in Itakura [22]. Quadrupolar arrays of dislocations were constructed by placing dislocations of antiparallel  $1/2\langle 111 \rangle$  Burgers vectors in an "S" arrangement [23], with initial displacements determined by anisotropic elasticity solutions. See figure 2, left. A quadrupolar arrangement minimises the stress each dislocation experiences in the simulation. These displacements were modified to be periodic, thereby removing artificial stacking faults which would appear between periodic images after introduction of the dislocation dipole. This was achieved by the subtraction of a linear error term from the superposition of displacement fields arising from the dislocations in the simulation cell and its periodic images [24]. To accommodate for the internal stress upon introduction of a dislocation dipole into the simulation cell, an elastic strain was applied to the cell, resulting in an additional tilt component to cell vectors [23, 24, 25]. Simulation cells were constructed with different initial core positions, which were sampled from the triangular region "EHS" (easy, hard and split) core positions, as detailed in figure 3. To fix the dislocation positions during relaxation, the three atoms surrounding the easy core, for each dislocation, were fixed in  $Z$  coordinate during relaxation, where  $Z$  is a  $\langle 111 \rangle$  direction, along the dislocation line. The k-point sampling mesh for each of these cells was  $5 \times 5 \times 30$ .

The interaction energy between the dislocation dipole and periodic images was defined differently to Itakura [22]. We followed the prescription of Bulatov and Cai [24] to find a regularised interaction energy, which is independent of truncation limit, in contrast to the formulas quoted in Itakura's papers. Details can be found in section 7.1.

The Peierls potential  $\Delta E_P^i$ , for an isolated dislocation at the  $i^{\text{th}}$  core position, can be calculated from

$$\Delta E_P^i = \Delta E_{\text{tbe}}^i - \Delta E_{\text{INT}}^i, \quad (1)$$

where  $\Delta$  refers to quantities, per dislocation, relative to the relaxed easy core configuration (labelled as E/1, as in figure 3). *e.g.*  $\Delta E_{\text{tbe}}^i = \frac{1}{2}(E_{\text{tbe}}^i - E_{\text{tbe}}^{\text{E}})$  is the difference in energy, per dislocation, between a relaxed cell which has the two dislocation cores placed at position  $i$ ,  $E_{\text{tbe}}^i$ , and a relaxed cell which has the two cores placed in easy core positions  $E_{\text{tbe}}^{\text{E}}$ , divided by the number of dislocations in each of the simulation cells. Dislocation-dislocation interaction energies are included in this term, due to dislocations in the simulation cell—and periodic images—interacting with each other, as can be readily seen in figure 2. To model the energy landscape of an isolated dislocation, these interaction energies must be subtracted, which is achieved by the correction term  $\Delta E_{\text{INT}}^i = \frac{1}{2}(E_{\text{INT}}^i - E_{\text{INT}}^{\text{E}})$ .

## 2.2 Preliminary calculations

To determine the binding energy of carbon to dislocations, we used the cluster method, as shown in figure 2, right. Simulation cells consisted of a cylindrical cluster of atoms, with a single dislocation introduced into the centre using displacements from anisotropic elasticity solutions. Each of the clusters were centred on the easy or hard core positions. The cluster of atoms was split into two regions: a central region of dynamic atoms with radius  $R_1$ , and an annulus of atoms, between  $R_1$  and  $R_2$ , which were fixed in position to the displacements from anisotropic elasticity.

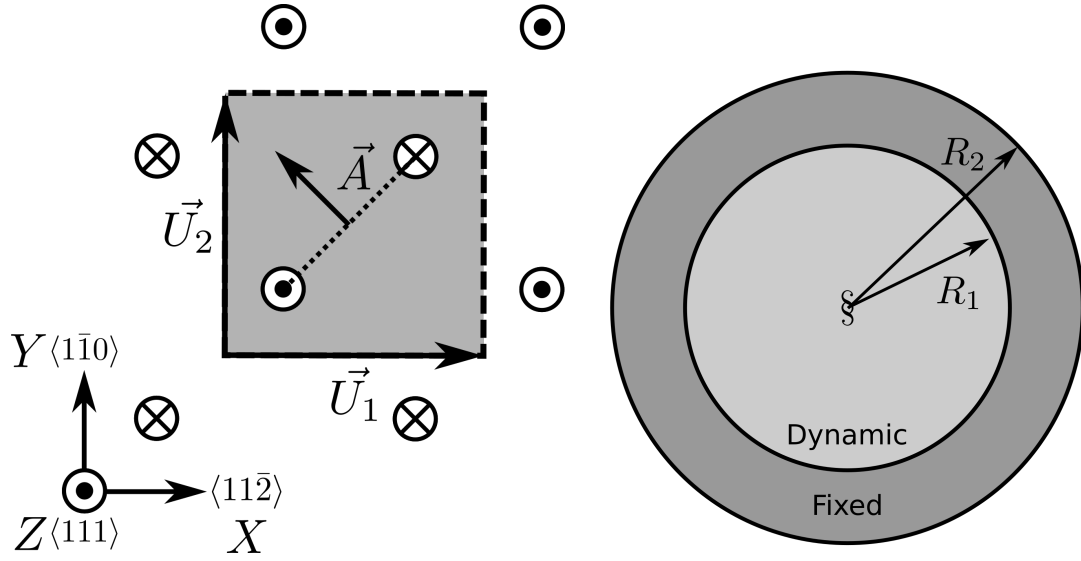


Figure 2: Schematics of dislocation simulation methods. Left: quadrupolar arrangement of dislocations in a simulation cell (grey square). This arrangement minimises the stress experienced by each dislocation in a periodic simulation. Cell vectors  $\vec{U}_1$  and  $\vec{U}_2$  are shown;  $\vec{A}$  defines the cut plane between the dipoles. The dislocation positions, and their corresponding burger's vector direction, are denoted by the symbols  $\otimes$  and  $\odot$ , which are antiparallel to each other. Tilt components added to cell vectors to accomodate for the plastic strain are not shown. Right: cluster method, where atoms are displaced according the displacement field from the screw dislocation at the centre of the cluster, denoted by " $\S$ ". Atoms in the annulus  $R_2 - R_1$  are fixed in position to the anisotropic elasticity solutions. Within  $R_1$ , all atoms can relax. Periodicity is only imposed in the  $Z$  direction.

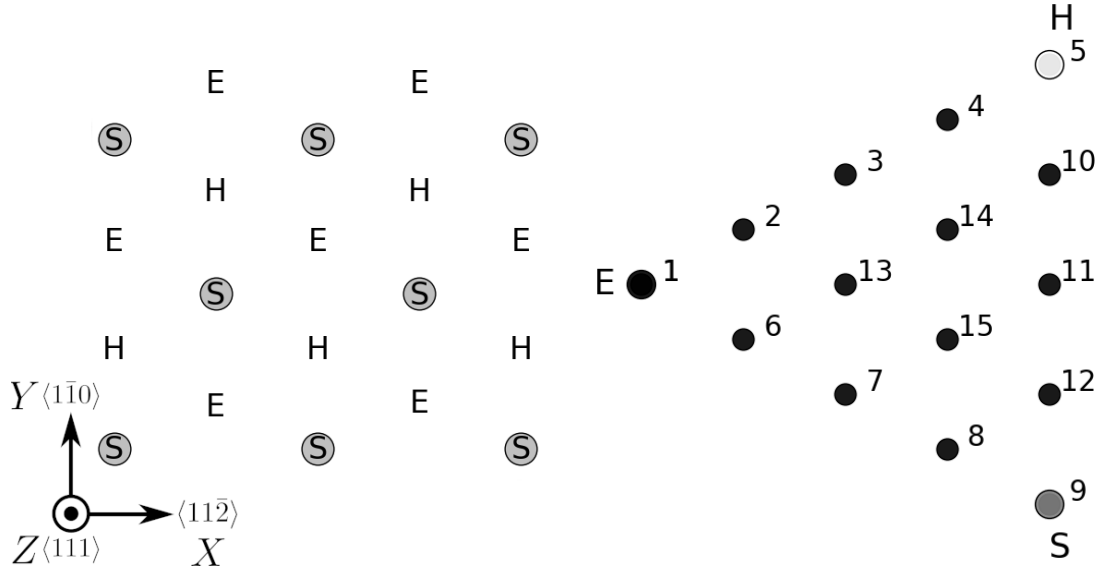


Figure 3: Diagrams of dislocation core positions. "E", "H" and "S" correspond to the easy, hard and split core positions respectively. Left: core positions as seen along the  $Z = \langle 111 \rangle$  direction, along the dislocation line. Atomic positions are shown as grey circles. Right: positions sampled within the triangle EHS used to determine the Peierls potential.

To confirm the anisotropic elasticity solutions were correct, we compared the displacements against the analytic solutions to the straight screw dislocation, as given in Hirth and Lothe [26]. Furthermore, energy scaling relations were verified. We inserted dislocations into cells of varying radii:  $R_1 = x\sqrt{2}a_{\text{bcc}}$ , and  $R_2 = (x + 1)\sqrt{2}a_{\text{bcc}}$ , where  $x \in \{2 \dots 5\}$ . The excess energy was defined as the energy difference of a cell with a dislocation inserted,  $E_d$ , with respect to a perfect cell reference energy of the same geometry,

$$E_{\text{excess}} = E_{\text{core}} + E_{\text{elastic}} = E_d - E_{\text{perfect}}, \quad (2)$$

where  $E_{\text{elastic}} = (\mu b^2/4\pi) \ln(R/r_c)$ , with  $R = R_2$  and  $r_c = b$ .

Initially, large cells of  $R_1 = 6\sqrt{2}a_{\text{bcc}}$ , and  $R_2 = 7\sqrt{2}a_{\text{bcc}}$  with depth of single burger's vector, were relaxed for both the easy and hard cores, which consisted of 522 and 540 atoms respectively. The three atoms surrounding the core were constrained to only relax in  $X - Y$  plane, to fix the dislocation upon relaxation. The k-point sampling mesh for each of these cells was  $1 \times 1 \times 24$ .

From the relaxed cells, a smaller region of 174 atoms, with  $R_1 = 3\sqrt{2}a_{\text{bcc}}$ , and  $R_2 = 4\sqrt{2}a_{\text{bcc}}$ , was cut from the dynamic regions. This smaller cell was extended to a thickness of  $3b$  in the  $Z$  direction. Carbon interstitials were inserted into octahedral sites near the dislocation core, in the middle layer. Exploiting reflection and rotational symmetry, only 10 interstitial sites needed to be used to obtain the binding energies of carbon  $\sim 2b$  from the core, denoted by  $iHj$  and  $iEj$ , where  $j \in \{1 \dots 10\}$ . The final binding sites are denoted by  $Hk$  and  $Ej$ , where  $k \in \{1 \dots 7\}$ . The three atoms surrounding the core in the first and third layers were again constrained to relax only in the  $X$  and  $Y$  directions. No such constraints were imposed on the middle layer.

Interestingly, if one to pre-emptively include the distortion carbon into the cell, by



superposing the displacement field generated from carbon in an otherwise perfect cell of 3b length—one does not find the true ground state structures, as predicted by dipole calculations which allow all degrees of freedom to be relaxed.

### 2.3 Fe-C binding energies

We calculated the carbon-dislocation binding energies as in Itakura [21].

The binding energy is given by

$$E_b = -(E_{d+C} + E_{\text{perfect}} - E_d - E_{C \text{ ref.}}), \quad (3)$$

where  $E_{d+C}$  is the total energy of a relaxed cluster with a carbon interstitial and a dislocation,  $E_d$  is the total energy of a relaxed cluster with a dislocation and  $E_{C \text{ ref.}}$  is the total energy of a relaxed perfect cluster with a single carbon in an octahedral site. A positive binding energy indicates favourable binding.

The zero-point energy (ZPE) is calculated as in Itakura. Details can be found in 7.2. The ZPE corrected binding energy is given by

$$E_b^Z = E_b + \Delta E_z,$$

where  $\Delta E_z = E_z - E_z^{\text{C ref.}}$  and  $E_z^{\text{C ref.}} = 202.5\text{meV}$  is the zero-point energy of carbon situated in an octahedral site in a perfect cluster of the same size.

Calculations were also

### 2.4 Carbon concentration on dislocation line

Using the Fe-C binding energies, one can predict the equilibrium carbon concentration of a carbon binding site  $c_d$ , using a thermodynamical mean-field model [27, 20, 28], under the assumption that carbon atoms around the core are sufficiently spaced such that intersite interaction energies are negligible.

The concentration is given by,

$$\frac{c_d^i}{1 - c_d^i} = \frac{c_{\text{bulk}}}{1 - c_{\text{bulk}}} \exp\left(\frac{-E_{\text{seg}}^i(c_d)}{k_B T}\right), \quad (4)$$

where  $i$  denotes the  $i^{\text{th}}$  carbon binding site.  $E_{\text{seg}}^i$  is the mean segregation energy defined as

$$E_{\text{seg}}^i(c_d) = -E_b^i + 2c_d V_{CC},$$

where  $E_b^i$  is the corresponding dislocation-solute binding energy (in the convention of attraction denoting a positive binding energy).  $c_d^i$  is the average concentration of the  $i^{\text{th}}$  carbon site bound to dislocations.  $c_{\text{bulk}}$  is the carbon concentration in the bulk, with  $c_{\text{nom}}$  the nominal carbon concentration per Fe atom.  $V_{CC} = 0.30\text{eV}$  is the carbon-carbon first-neighbour repulsion term, which is calculated as in Ventelon [20]. This repulsion term was calculated from carbon in the H1 prismatic site. It was assumed that this repulsion term is the same for carbon in the E2 site.

In a given volume  $V$ , the number of carbon sites along the dislocation cores is given by  $N_d = \rho V/b$ , with  $\rho$  the dislocation density, and the number of octahedral sites is  $N_{\text{oct}} = 6V/a_{\text{bcc}}$ . This imposes constraints on the carbon concentrations:  $N_{\text{oct}}c_{\text{bulk}} + N_dc_d = N_{\text{oct}}c_{\text{nom}}/3$ , where the factor of 3 is because there are three octahedral sites

per Fe atom in the bcc lattice. Using this relation, equation (4) can be solved self-consistently to give the carbon concentration around the core, as a function of nominal carbon concentration and temperature. The nominal carbon concentration was taken to be the maximum solubility of ferrite in the DER region, 0.02 wt%  $\approx$  1000 appm [17]. Calculations of 10 and 500 appm were also performed. The dislocation density was varied between  $1 \times 10^{12}$ ,  $1 \times 10^{14}$  and  $5 \times 10^{15}$ , to see the effects of low densities up to the upper bound of dislocation densities  $\sim 5 \times 10^{15}$  found in Fe-0.61wt%C martensite [29].

Further discussion on carbon concentration formulations is given in section 2.5.2.

## 2.5 Line Tension Model

The kink-pair formation enthalpy is defined as the minimum energy necessary to create a kink-pair from a dislocation in a Peierls valley. One can find this by sampling the energy landscape seen by a dislocation line which moves one peierls valley to the next, from which the minimum enthalpy path can be sought. The difference between the maximum enthalpy image, corresponding to a dislocation configuration in a transition state, and enthalpy of the initial state, is the kink-pair formation enthalpy. One can efficiently determine the minimum enthalpy path using the String/Nudged Elastic Band (NEB) algorithms. In these methods, a set of images, which interpolate between the initial and final states, are relaxed along the energy landscape.

From atomistic calculations of the Peierls potential and carbon-dislocation binding energies, one can construct a line tension model of a dislocation from which we can obtain the kink-pair formation energies as a function of stress and carbon content [26, 22, 21]. This model views the dislocation as an elastic chain which moves in the Peierls potential  $\Delta E_P$ . Models of this type—consisting of a one-dimensional chain of particles with spring force interactions between nearest-neighbours, in a substrate potential—are also called Frenkel-Kontorova models, and have been crucial in some of the first investigations into kink-pair formation, among other non-linear processes [30, 31, 32, 33].

The dislocation is modelled as a discretised line, with layer labels  $j$ . The energy of the dislocation line is given by:

$$E_{LT} = \frac{K}{2} \sum_j (\vec{P}_j - \vec{P}_{j+1})^2 + \sum_j \Delta E_P(\vec{P}_j) + (\sigma \cdot \vec{b}) \times \vec{l} \cdot \vec{P}_j - \sum_{j,k} E_C(|\vec{P}_j - \vec{P}_k^C|),$$

where  $K$  is a constant calculated from atomistics,  $\Delta E_P$  is the Peierls potential,  $\sigma$  is the stress applied and  $\vec{b}$  is the burger's vector, with the dislocation line sense given by  $\vec{l}$ .  $\vec{P}_j$  corresponds to the dislocation core position in a given layer.  $E_C(|\vec{P}_j - \vec{P}_k^C|)$  is the binding energy of a particular carbon  $k$ , at position  $\vec{P}_k^C$ , to a dislocation core positioned at  $\vec{P}_j$ . The kink-pair formation enthalpy can then be found using the string method to relax images which interpolate between the initial and final states (straight dislocations in adjacent peierls valleys), to find the height of the transition-state barrier. A `julia` implementation of the string algorithm, accelerated by use of an ODE solver, was used to relax the images [34]. The implementation was validated on the dataset of Itakura [22].

### 2.5.1 Line-tension model in carbon environment

Dislocations form Cottrell atmospheres of carbon, which influence their motion. Analysis of the dynamics of a dislocation moving from one Peierls valley to the next, in an environment of carbon in equilibrium with the bulk, can provide estimates of: the mean energy barrier experienced by a straight dislocation segment upon glide, and the mean kink-pair formation enthalpy, both as functions of nominal carbon concentration. Results of the latter can be used as inputs to a self-consistent kinetic Monte-Carlo (SCKMC) model of dislocation glide, which has been shown to predict dislocation structures in hydrogen-charged iron [35]. The kink-pair formation enthalpy calculations in this paper study were performed in the limit of slow dislocation glide, allowing carbon to equilibrate between sites, however more accurate results may be possible by accounting for dislocation velocity in a self-consistent manner.

The binding sites of carbon around the easy and hard core dislocation positions were found from atomistic simulations, detailed in section 3.3. Movement of a dislocation between Peierls valleys generates intermediate core positions which lie between the easy and hard cores. Carbon trap sites are not well-defined for these intermediate dislocation positions. To circumvent this, trap site positions were smoothly mapped between the easy and hard core positions by use of the dislocation core coordinate  $P_x$ . Further information on the mapping of sites can be found in appendix .

The carbon concentration on the dislocation line was calculated by the self-consistent thermodynamical mean-field model, detailed in 2.4. The concentration was fixed to the value obtained using the H1 binding energy,  $c_{\text{total}} = c_d^{\text{H1}}$ , imposing the assumption that the dislocation neither rejects or absorbs carbon, despite changes in the carbon environment upon core movement. Thus carbon concentration on the dislocation line remained in equilibrium with the bulk during the simulations.

The equilibrium concentration of carbon in a trap site  $i$ ,  $c_i^e$  was initially determined by use of Maxwell-Boltzmann statistics [26], as done by Cottrell and Bilby [36], and Gong [35],

$$c_i^e(x) = c_d^{\text{H1}} \frac{e^{-E_i(x)/k_b T}}{\sum_j e^{-E_j(x)/k_b T}}.$$

These concentrations modify the interaction energy of a given site multiplicatively, such that the total interaction energy of a dislocation in an environment of solutes is given by

$$E_{\text{INT}}^e = \sum_j c_j^e E_j(x).$$

Kink-pair formation enthalpies were obtained using the string method, as detailed in section 2.5.

### 2.5.2 Extension to more Fermi-Dirac statistics

Cottrell and Bilby’s assumption of Maxwell-Boltzmann statistics, as seen in equation (2.5.1), is valid for small dislocation-solute binding energies, which are generally found for solutes far from the dislocation [37]. However, close to the dislocation core, we expect a strong binding of carbon to dislocations, as such, Maxwell-Boltzmann statistics fails to be a good description of carbon occupancies: one finds unphysically large occupancies, due to carbon being able to occupy the same site.

For a more realistic description of carbon occupancies, one must account for the limited number of carbon sites close to the dislocation core, which are either occupied or not. This problem, of distributing indistinguishable particles (neglecting inter-/intra-site interactions) between sites which can only be singly-occupied, is reminiscent of Fermi-Dirac statistics, which was applied by Nematollahi [38] to treat carbon occupancies around an easy core up to a cut off of 0.04—a result obtained by the EAM calculations of Veiga [39]. This distribution was assumed to be true, however, it neglected the effect of assumptions which were not explicitly taken into account. Louat [40] provided a more rigorous derivation for the concentration of solutes close to the dislocation core, which has been used by many in recent years [41, 20, 37, 27, 28]. In this formulation, it is assumed that the area around the dislocation is divided into a number of sub-regions (an effective lattice) where only one solute atom can occupy each position, and there are no inter-line or inter-site interactions. One only accounts for the configurational entropy of the effective lattice; electronic, vibrational and magnetic entropic contributions are not taken into account [20]. This treatment of configurational entropy becomes inaccurate for low binding energies, as noted the case of hydrogen/hydrogen-vacancy complexes in Fe [42]: with low enough binding energies, the species is able to move in a smooth and continuous potential, resulting in a larger configurational phase space available than just the sampled binding sites taken into. We expect due to the large binding energy of carbon to dislocations, relative to hydrogen, for a range of distances, the configurational entropy would not be significantly enhanced compared to the lattice model.

## 3 Results

### 3.1 Peierls Potential

Comparison of 2d Peierls potentials of the  $1/2\langle 111 \rangle$  screw dislocation between DFT and tight-binding models can be found in figure 4, with data found in table 1. The sampled energies were interpolated using 2d cubic splines. The relative energies between the different core positions was found to be smaller in both tight-binding models compared to DFT. These are artifacts of the models, which have been reproduced in atomistic NEB calculations of the  $1/2\langle 111 \rangle$  screw dislocation Peierls barrier using the canonical  $d$ -band model: the Peierls barrier in this model is approximately half that of DFT [43].

The Peierls potential of the  $d$ -band model was found to be more reminiscent of DFT, compared to the  $s$ - $d$  model; but the deviation is small: the maximum difference between the  $d/s$ - $d$  models being  $\sim 10$  meV, with the  $d$ -band model being, on average,  $\sim +3$  meV higher.

The split core energy is lower than that of the hard core, which is reminiscent of EAM potentials [22], but not as severe, as seen in figure 5. Some of this discrepancy can be attributed to the erroneous interaction term included by Itakura, as detailed above—interaction energies can become arbitrarily high, if not made independent of truncation limit—but likely there are effects in DFT which are not encapsulated fully within the tight-binding description, such as a lack of core electron repulsion upon deformation of the lattice, which would increase the relative energy difference. Consequences of this discrepancy on future kMC simulations are discussed in section 4.

The transitional kink shape from the  $s$ - $d$  and  $d$ -band Peierls potentials may differ compared to DFT, with dislocation core positions possibly being situated closer to the split core position, similar to EAM potentials [22, 44]. Following the Peierls potential along the H-S direction, as seen in figure 5, we see that the Itakura potential has a

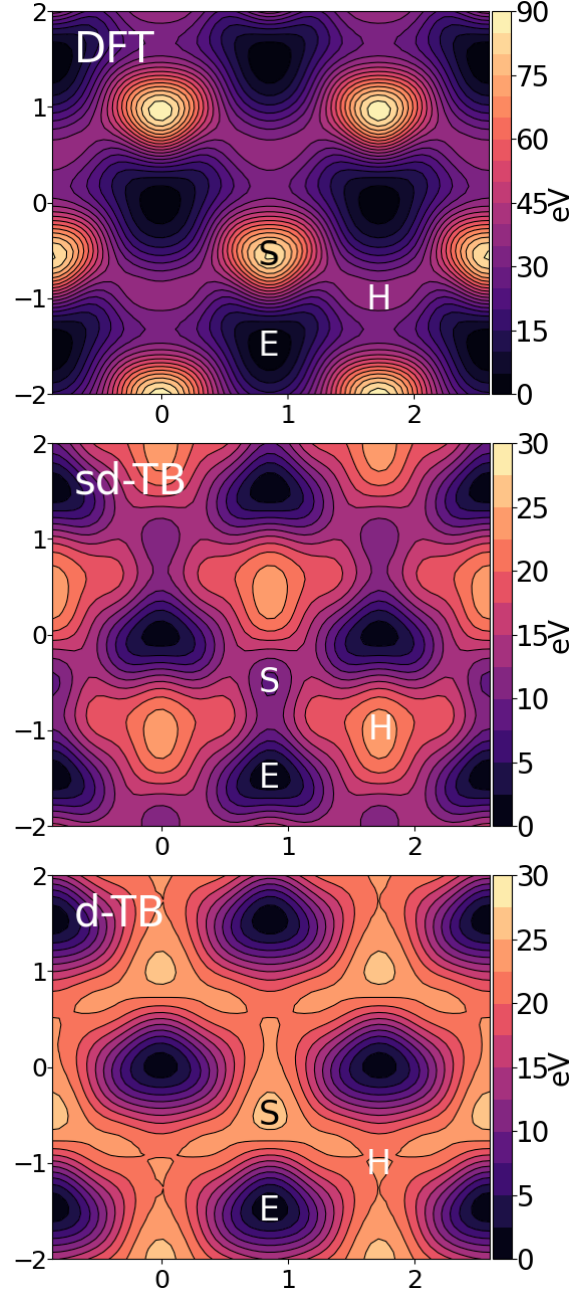


Figure 4: Comparison of 2d Peierls potentials of the  $1/2\langle 111 \rangle$  screw dislocation between DFT [22] (top) and tight-binding ( $sd$  non-orthogonal middle, canonical  $d$ , bottom).  $x-y$  axes in units of  $d = a\sqrt{2}/3$ . Energy scale is in meV. "E", "H" and "S" correspond to easy, hard and split core positions respectively, with the latter also corresponding to atomic positions. The relative energies between the different core positions is smaller in tight-binding compared to DFT. The split core as seen in tight-binding is reminiscent of EAM potentials, where the split core energy is lower than that of the hard core. The discrepancy is probably due to an insufficient repulsion at close range within the tight-binding model.

Table 1: Table of energies used to calculate the Peierls potential. All values in meV.  $\Delta E_P^{\text{DFT}}$  values taken from [22].

Pos	$\Delta E_{\text{INT}}$	$\Delta E_{\text{tbe}}$	$\Delta E_P^{sd}$	$\Delta E_P^d$	$\Delta E_P^{\text{DFT}}$
1	0	0	0	0.0	0
2	-0.7	7.3	7.9	6.3	3.2
3	-1.4	16.0	17.4	15.1	19.2
4	-2.0	22.2	24.2	20.4	31.1
5	-2.5	24.8	27.4	22.6	39.3
6	-3.3	3.0	6.3	4.6	11.5
7	-6.5	7.1	13.6	12.7	39.9
8	-9.6	13.0	22.6	22.7	75.2
9	-12.5	5.4	17.9	26.8	108.9
10	-4.8	22.1	26.9	23.0	34.8
11	-7.2	18.2	25.4	23.5	37.9
12	-9.8	14.0	23.8	24.4	60.7
13	-3.8	11.5	15.3	13.2	17.6
14	-6.9	15.1	22.0	20.3	29.9
15	-4.3	18.6	22.9	20.0	39.7

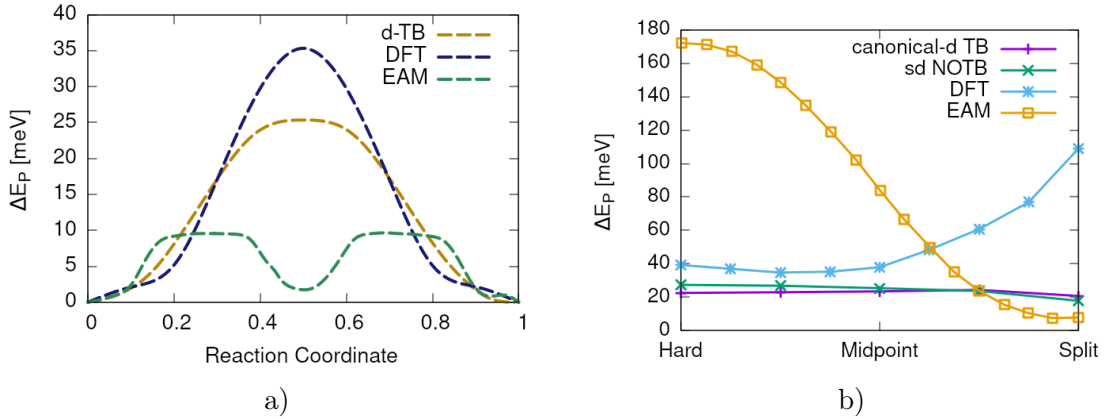


Figure 5: Left: Peierls barriers from atomistic calculations using canonical- $d$ -band tight-binding, DFT and the Mendelev EAM potential, plots of the corresponding dislocation pathways can be found in figure 13. The EAM potential of Mendelev [44] has an unphysical well in the centre of the potential, while tight-binding and DFT produce single-humped potentials. Right: Peierls potential along the hard-split line. One can see in  $s$ - $d$  tight-binding model pathway is similar in shape to the EAM potential of Mendelev [44]: it decreases consistently from the hard core to the split core. In DFT one finds a saddle point between the hard core and the midpoint.

saddle point minimum, which corresponds to the dislocation core positions found upon kink-pair formation [22]. In the  $s$ - $d$  model, the Peierls potential decreases monotonically along the H-S line and there is a subtle maximum found in the  $d$  – band model. This data suggests there may be a deviation in the dislocation path found in DFT, in moving from one peierls valley to the next along the H-S line. Atomistic calculation of the Peierls barrier between two easy core positions in the canonical  $d$ -band model found core positions of the transitional kink state to go through the metastable point, similar to DFT [43], which suggest the deviation may not be severe. Section 3.5 discusses the effect the Peierls potential has on the pathway taken by a dislocation moving from one Peierls valley to the next.

### 3.2 Preliminary calculations

To validate the cluster simulation method, the excess energy, defined as the difference in energy between a cell with a dislocation, and a perfect reference cell, was plotted as a function of  $\ln(R/r_c)$ , where  $R = R_2$  of the cluster and  $r_c = b$ , as seen in figure 6. In isotropic elasticity theory, this should give a linear dependence where the gradient corresponds to  $\mu b^2/4\pi$ , with the  $y$  intercept corresponding to the core energy  $E_{\text{core}}$ . This is well reproduced by our model, except at low  $\ln(R/r_c)$  as expected, where the cell size is not large enough to accommodate for sufficient relaxation of the dislocation core, increasing the core energy, which is not accounted for in elasticity theory.

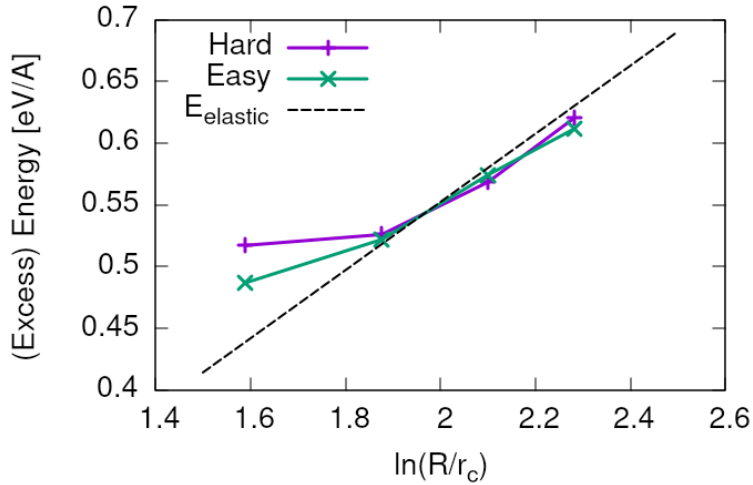


Figure 6: Excess energy of dislocation clusters with differing radii for both the easy and hard core configurations. The prediction from elasticity theory is given by the black, dashed line. Deviation of both cores occur when cell size is small, creating an increase in the core energy, which elasticity theory cannot account for.

The energy cost to transform from the easy to the hard core can be estimated by the difference in excess energies between the cores in the limit of  $\ln(\frac{R}{R_0}) \rightarrow 0$ . At the smallest measured value, one finds that the core energy difference  $\Delta E_{\text{core}}^{\text{Easy-Hard}} = 76$  meV/b, which is in good agreement with the DFT value of 82 meV/b [22].

For a line tension model of a dislocation, it is necessary to ascertain the energy, denoted  $E_L = E_{\text{el}} + E_{\text{core}}$  as in Provile [33]. This can be obtained by subtracting the total energies of relaxed dislocation configurations to obtain the core energy.

### 3.3 Fe-C binding energies

As found in DFT simulations by Ventelon [20], when a carbon was placed in the vicinity of a relaxed easy dislocation core—in either of the two nearest, distinguishable, octahedral sites—a spontaneous reconstruction of the dislocation core occurred: from easy to hard. Upon reconstruction, the dislocation core moved to a neighbouring triangle, when looking along the  $\langle 111 \rangle$  direction, where the carbon found itself situated in the centre. This will be called a prismatic site, as in Ventelon’s paper. This confirms that both hard and easy dislocation cores must be studied to fully understand screw dislocation behaviour in bcc iron.

The binding energies of carbon to both the hard and easy cores can be seen in table 3, with the resulting distribution of carbon in figures 7 and 8. The distribution of carbon strongly depends on the type of core it finds itself situated near. The easy core only significantly modifies the position of the iE1 site, to the E1 site, situated in the centre of an adjacent triangle. All other sites are unaffected, so there is a one-to-one correspondence between all iE $j$  and E $j$  sites, where  $j \in \{2 \dots 10\}$ . There are carbon basins available close to the triangular region containing the core, but not inside.

Carbon favours a prismatic site within the hard core (H1), which has the highest binding energy, 1.29 eV, of all sites considered. There are no binding sites apparent in a triangular annulus (of width  $a_{\text{bcc}}\sqrt{2}/2$ ) surrounding the hard core triangle due to the destruction/volume reduction of octahedral sites near the hard core. The initial octahedral sites, iH1 and iH2 decay to the H1 site. Similarly, iH3 and iH4 decay to the H2 site, with iH9 and iH10 decaying to a H7 site. Relations between each of the sites is given in table 2.

Table 2: Decay relations between the initial and final sites upon relaxation of carbon interstitials around the hard core.

Initial	Final
iH1, iH2	H1
iH3, iH4	H2
iH5	H3
iH6	H4
iH7	H5
iH8	H6
iH9, iH10	H7

Note that interactions between carbon atoms around the core are not taken into account here: figures 7 and 8 are purely diagrammatic and not what one expects the true distribution of carbon around a screw dislocation would be. Carbon is strongly repulsive at first nearest-neighbour distances, which would modify each of these distributions.

These binding energies agree well with experiment and atomistic/elastic calculations. EAM simulations by Clouet [45, 46] found a maximum binding energy of 0.41 eV by calculating the elastic dipole tensor within Eshelby theory. Hanlunyuang et al. [47], similarly conducted DFT and EAM calculations for the interaction energy 12Å from the core, and their calculations agreed with the continuum limit of Eshelby theory with a binding energy of 0.2 eV. In DFT calculations by Ventelon [20], the interaction energy of a carbon in a hard core prism configuration was found to be 0.79 eV for a thickness in the  $Z$  direction of  $3b$  (0.73eV for  $6b$ )—in the convention that a positive binding energy indicates attraction. This is significantly lower than the 1.29eV interaction energy of



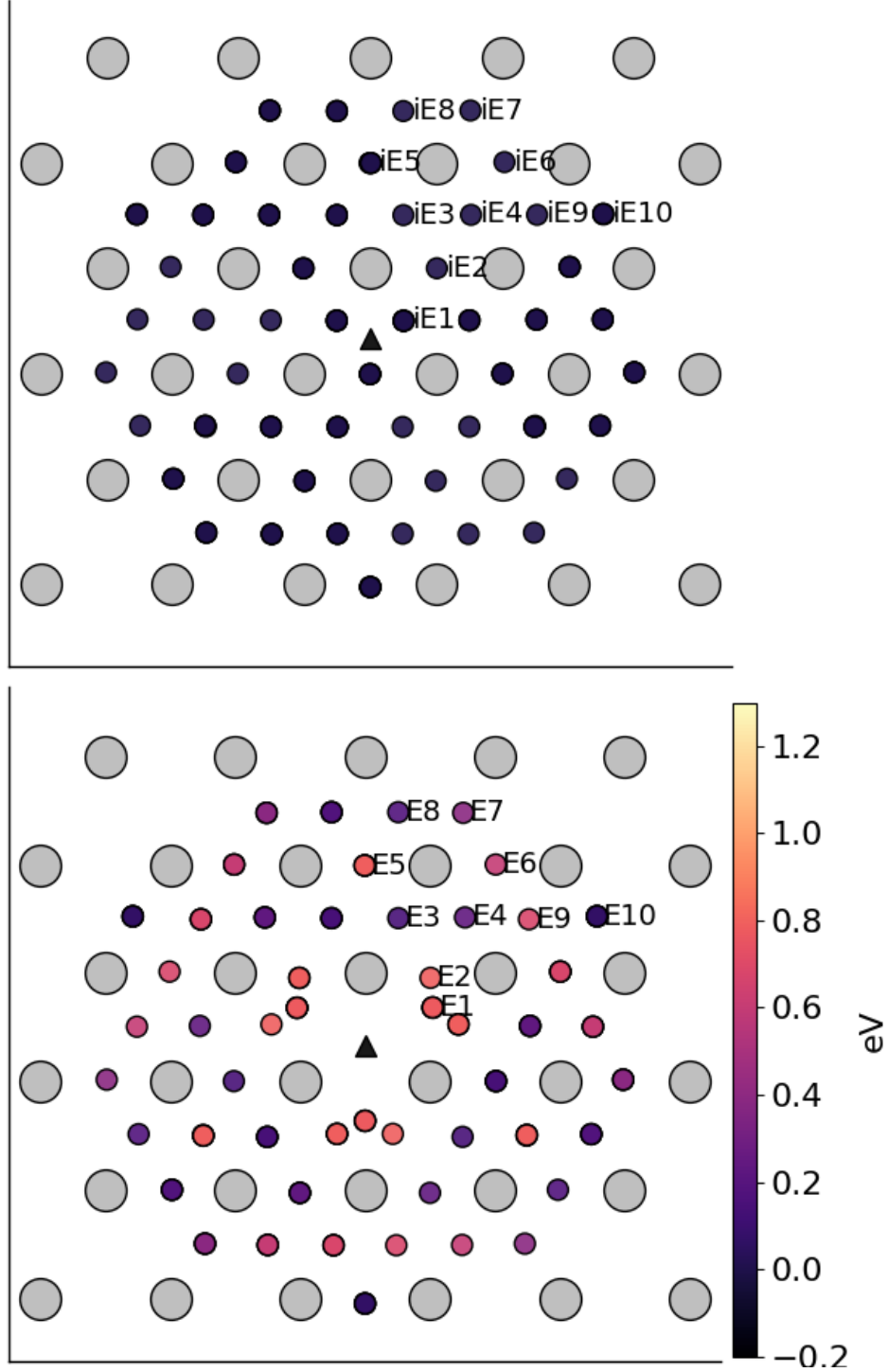


Figure 7: Initial (top) and final (bottom) positions and binding energies (eV) of carbon around the easy core. Binding energies are not shown for the initial positions. Top: initial positions before relaxation. Bottom: final positions and binding energies after relaxation. The core was constrained by fixing the top and bottom three atoms surrounding each of the cores. As shown by Ventelon [20], the first and second closest octahedral sites to the hard core decay to a prismatic position inside the hard core.

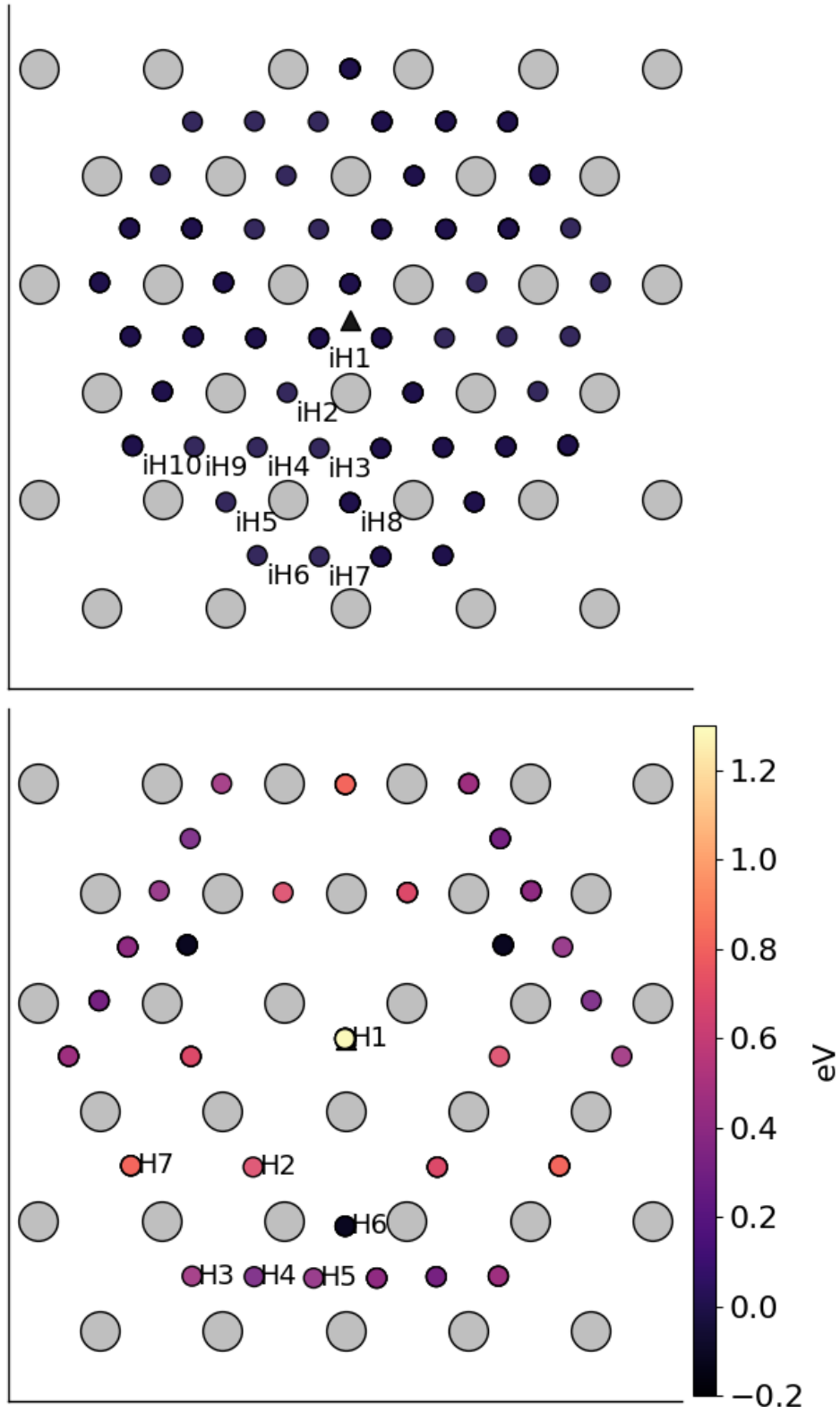


Figure 8: Initial (top) and final (bottom) positions and binding energies (eV) of carbon around the hard core. The core was constrained by fixing the three atoms surrounding each of the cores in the top and bottom layers. As shown by Ventelon [20], the first and second closest octahedral sites to the hard core decay to a prismatic position inside the hard core.

Site Type	distance from core [b]	$E^z$ [eV]	$\Delta E^z$ [eV]	$E_b$ [eV]	$E_b^z$ [eV]
E1	0.57	0.185	-0.018	0.793	0.775
E2	0.70	0.202	-0.001	0.793	0.793
E3	0.99	0.205	0.002	0.137	0.139
E4	1.21	0.208	0.005	0.229	0.234
E5	1.36	0.210	0.008	0.784	0.791
E6	1.66	0.209	0.007	0.597	0.603
E7	1.89	0.206	0.003	0.385	0.388
E8	1.77	0.203	0.000	0.177	0.178
E9	1.52	0.201	0.000	0.683	0.683
E10	1.95	0.202	0.000	0.067	0.067
H1	0.00	0.196	-0.006	1.298	1.291 [ 0.881 <sup>a</sup> , 0.790 <sup>b</sup> ]
H2	1.19	0.210	0.007	0.691	
H3	2.12	0.209	0.007	0.461	
H4	1.91	0.207	0.005	0.311	
H5	1.80	0.208	0.006	0.403	
H6	1.40	0.207	0.005	-0.119	
H7	1.35	0.206	0.006	0.825	

Table 3: Table of energies leading to the zero-point energy corrected binding energy using the cluster method for simulation of dislocation-carbon interactions. <sup>a</sup> Tight-binding quadrupolar array results, starting from a fully relaxed easy core quadrupole extended to a depth of 3b with carbon introduced into the iH1 site in the middle layer, by both dislocations. <sup>b</sup> DFT results of Ventelon, using the same quadrupolar configuration as in <sup>a</sup>. In both quadrupolar simulations, carbon ended up in the H1 site.

tight-binding. This discrepancy can be partially explained by the fact that the cells have not been allowed to relax with all degrees of freedom, as in the Ventelon results: the three atoms around the screw core are fixed in  $Z$  so the dislocation core position does not change upon relaxation.

Repeating the calculation for the binding of a H1 carbon to a screw dislocation using a quadrupolar array, allowing for all atoms to relax, gives a binding energy of 0.88 eV. This agrees very well with the DFT results of Ventelon [20].

A source of error for this discrepancy is likely from the fitting of the tight-binding model itself. The Peierls barrier of this  $s$ - $d$  model of iron, necessary for Fe-C interactions, has been shown to be half that found in DFT [43], but the solution energies for Fe-C defect complexes are well described. This implies there is insufficient repulsion between Fe-Fe species upon deformation, leading to a larger resultant Fe-C binding energy from tight-binding.

### 3.4 Carbon concentration along on line

The variation of carbon concentration along the dislocation line for the highest binding energy sites of the easy and hard cores can be seen in figure 9. We see at low temperatures, all dislocations are decorated with carbon. As temperature increases, the amount of carbon decorating the dislocations starts to decrease. Due to the lower binding energy of carbon to the easy core, desaturation occurred at a lower temperature compared to the hard core. Dislocation densities near the upper bound of what has been observed in martensite,  $\rho \approx 10^{15}$ , reduce the temperature at which carbon concentration starts to decrease on the dislocation core. Lower nominal carbon concentrations cause carbon concentrations around the dislocation to decrease at a lower temperature.

In the high-purity iron case,  $C_{\text{nom}} = 10$  appm, we find at dislocation densities above  $\rho \approx 10^{15}$ , that there is a reduction in the maximum concentration permitted in the material, with increasing dislocation density. This is due to the fact that there is not enough carbon for all of the dislocations, as such the concentration on the dislocation line drops.

In the operating temperature range of  $40 - 90 \text{ deg C} = 310 - 360 \text{ deg K}$ , we expect most hard core sites are saturated. Given the high concentrations of the E1/E2 sites around the easy core in this range, we expect all dislocations will be of the hard core type, due to reconstruction of the easy core by the adjacent carbon.

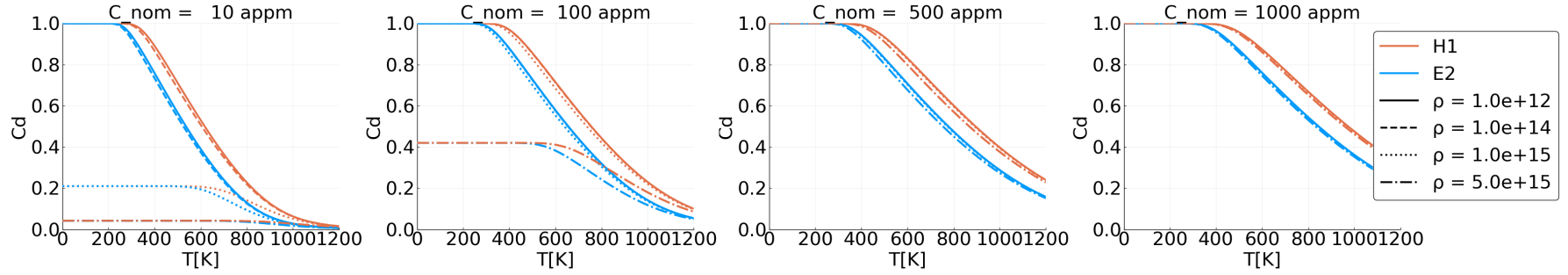


Figure 9: Variation of carbon concentration on the dislocation line  $c_d$  for the highest-energy binding sites for the hard core (H1) and easy core (E2). Solid, dashed, dotted and dash-dotted lines correspond to dislocation densities of  $1 \times 10^{12}$ ,  $1 \times 10^{14}$ ,  $1 \times 10^{15}$  and  $5 \times 10^{15}$  respectively. The nominal carbon concentrations are 10, 100, 500 and 1000 appm from left to right, where around 1000 appm corresponds to the concentration of carbon at the solubility limit of C in ferrite: 0.02wt%.  $c_d$  and  $c_{\text{bulk}}$  reached self-consistency, with an absolute tolerance of  $1 \times 10^{-6}$ . C-C interactions were taken into account with the repulsive first-neighbour interaction energy  $V_{\text{CC}} = 0.30$  eV. No intersite interactions were taken into account. The maximum concentration of carbon around the easy core, drops off at a lower temperature than that of the hard core due to lower binding energy of the E2 site compared to the H1 site. The operating temperature is taken to be 50 deg C = 320 deg K.

### 3.5 Line Tension Model

\* Insert here what the line tension model neglects in terms of energetics \*

#### 3.5.1 Prerequisites

The  $K$  coefficient for the line tension model was calculated from atomistic simulations, using the method of Itakura [22], by calculation of a Hessian from the displacement of atoms surrounding the dislocation core. Tight-binding gave  $K = 0.734 \text{ eV}\text{\AA}^{-2}$ , which agrees well with DFT, where  $K = 0.816 \text{ eV}\text{\AA}^{-2}$ .

||

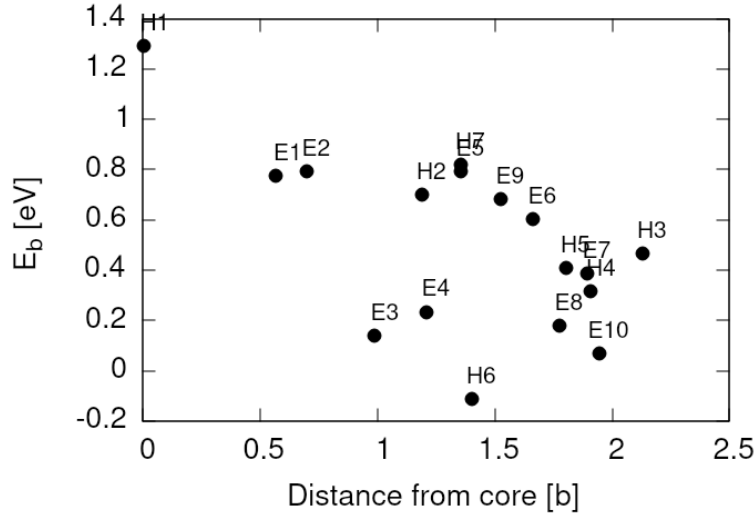


Figure 10: Distance dependence of the binding energies of carbon to the  $1/2\langle 111 \rangle$  screw dislocation in iron. Positive binding energies denote a favourable binding.

Dislocation-carbon binding energies were found to decay with distance, as seen in figures 10 and 11. A Lorentzian was fit to specific binding energies such that a continuous function could be used to describe binding within the line tension model. This is a purely empirical model. The choice of sites used for the fitting is discussed in section 4.

This distance-dependence agrees well with previous calculations of the binding energy at larger distances from the core [47].

#### 3.5.2 Kink-pair formation in pure iron

In figure 12, one can see the  $P_x$  and  $P_y$  core positions which result from the highest enthalpy image of kink-pair formation for the canonical- $d$  and  $sd$  tight-binding models, where the DFT comparison is from [22]. Plots of the corresponding dislocation core pathway,  $P_j = (P_x^j, P_y^j)$ , looking down the dislocation line, are shown in 13.

The  $P_x$  line shape agrees well with the DFT-based results. The kink width was found to be slightly wider:  $W_k \sim 11b$  in tight-binding from the line-tension model, compared to  $10b$  in DFT and atomistic tight-binding results [43]. The larger width from tight-binding compared to DFT results from the width being proportional to  $b\sqrt{K/\Delta E_P}$  [22], with the discrepancy between the  $K^{\text{tbe}}$  and  $K^{\text{DFT}}$ , being smaller than that of the Peierls potential. Differences in the  $P_y$  line shape are noticeable, with the canonical- $d$  model reproducing the result closest to the DFT  $P_y$  line shape.

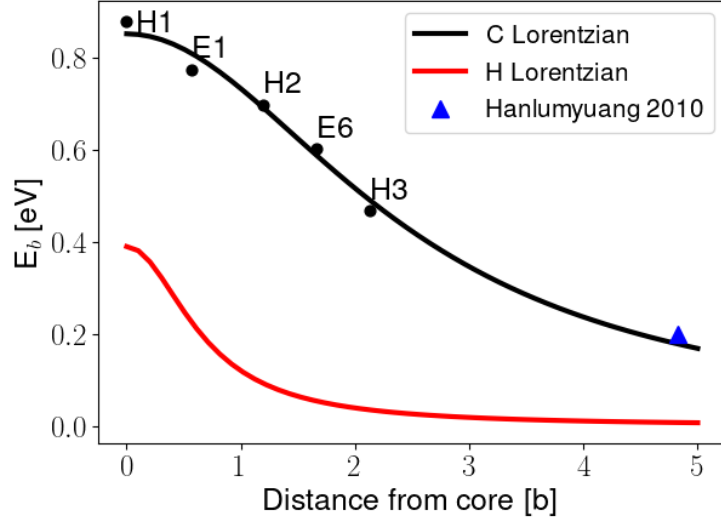


Figure 11: Parameterised distance dependence of carbon binding energies to the  $1/2\langle 111 \rangle$  screw dislocation in iron. The sites chosen to fit to were determined by those sites a prismatic carbon in a hard core configuration would find itself, if the dislocation were to move without it along the  $X = \langle \bar{2}11 \rangle$  direction. The triangle, labelled Hanlummyuang, refers to the binding energy resulting from measurement of the elastic dipole tensor from DFT calculations evaluated at 12 [47]. Binding energy of hydrogen to the  $1/2\langle 111 \rangle$  screw dislocation also shown for comparison [21]

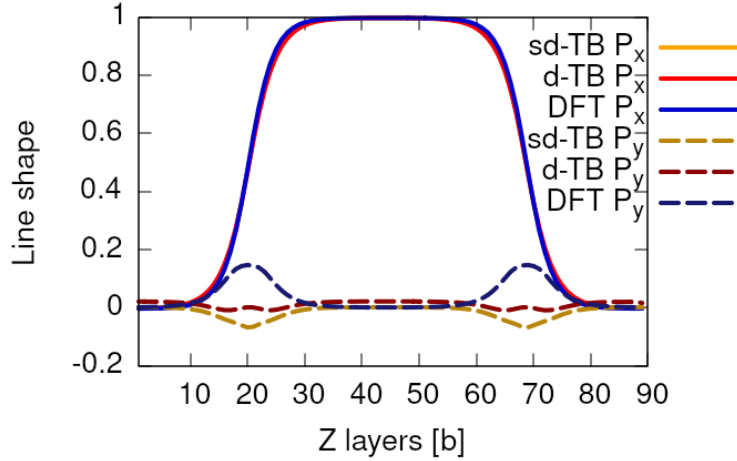


Figure 12: Core positions of the line tension model from DFT (blue) and tight-binding (yellow) for the middle image corresponding to the MEP and the kink-pair formation energy. Images were relaxed using the ODE String method of Makri and Ortner [34].  $P_x$  and  $P_y$  correspond to the x/y-coordinate of the dislocation core position in each of the discretised layers of the dislocation. One finds that the kink width in tight-binding is wider than that found in DFT, which corresponds with the fact that the width is proportional to  $b\sqrt{K/\Delta E_P^{\text{tbe}}}$ , where the reduction in  $\Delta E_P^{\text{tbe}}$  is greater than the reduction in  $K_{\text{tbe}}$ .

The differences in line shapes manifest themselves clearly in plots of the dislocation pathway, figure 13, where we see the path a dislocation takes looking down the dislocation line. The core pathway dips below the midline in both the  $d$  and  $sd$  models, with a more pronounced effect being shown by the  $sd$  model. Apart from this discrepancy, we see there is good agreement between tight-binding to DFT when compared to the EAM potential of Mendelev [44] in which we see a path which passes close to the split-core position. This is expected due to the low value of the Peierls potential of the EAM, as seen in figure 5.

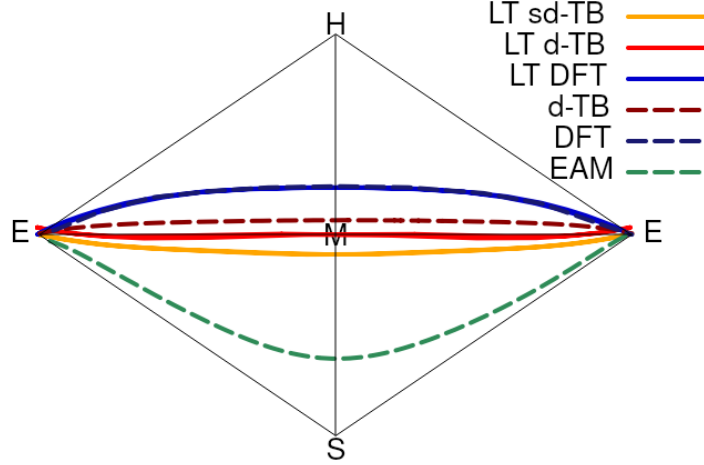


Figure 13: Comparison of minimum energy pathways from different atomistic calculations to the line-tension model. Dashed lines correspond to atomistic calculations. Solid lines are results from the line-tension models. Tight-binding follows a pathway much closer to that of DFT. EAM potentials predict that the dislocation core goes to the split core and then back to the easy core. Even though the Peierls landscape found in tight binding has similar characteristics to the EAM in terms of the energetic ordering of different core states, the description of the minimum energy pathway of the  $1/2\langle 111 \rangle$  screw dislocation as it moves between core positions is in good agreement with DFT.

The kink-pair formation enthalpies obtained from the tight-binding models can be found in table 4. Tight-binding underestimates the kink-pair formation enthalpy by 0.18 eV, in comparison to DFT. This can largely be attributed to the difference in Peierls potentials between DFT and tight-binding.

Table 4: Kink-pair formation energies between DFT, and the two flavours of tight-binding used with the line-tension model .

Method	$H_k$
DFT	0.71 eV
TB (sd-non-orthog.)	0.56 eV
TB (d-orthog.)	0.53 eV



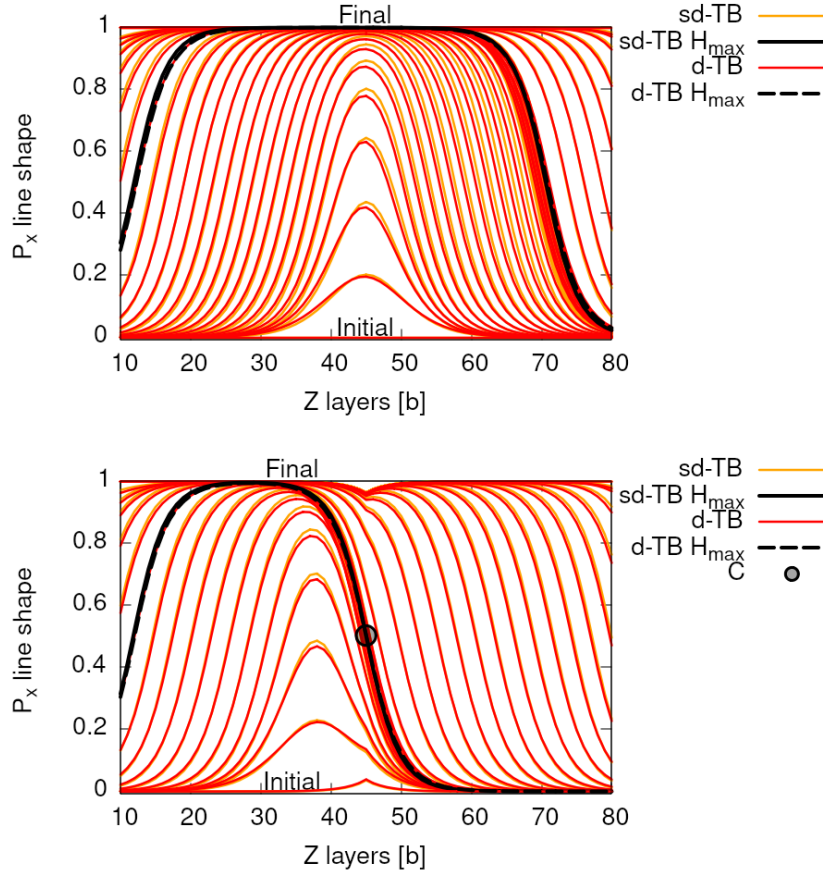


Figure 14: Comparison of  $P_x$  lineshapes for the  $sd$  and  $d$  models in pure iron (top) and iron with a single carbon interacting with the central dislocation segment in E1 site (bottom). The highest enthalpy images,  $H_{max}$ , for each of the models are shown in black. In pure iron, the  $d$  model lineshapes are offset from the  $sd$  due to the different Peierls potentials involved. With carbon along the path of migration, we find the dislocation intersects the solute, due to its large binding energy.

### 3.5.3 Kink-pair formation enthalpy with a single carbon

To understand how kink-pair nucleation is affected by carbon, one can study the formation of a kink-pair but with the additional interaction of a single carbon ahead of the dislocation.

We place carbon in the E1 site, the highest binding energy site of carbon to the easy dislocation core. The carbon is fixed in place during kink-pair formation, as such we are assuming a regime in which the dislocation velocity is much greater than the diffusion of carbon. Carbon-dislocations interactions are only permitted between the dislocation segment closest to the carbon.

$P_x$  line shapes obtained during kink-pair formation can be seen in figure 14. The addition of carbon causes a cusp in the dislocation line towards the carbon in the initial and final images, due to the reduction in potential the central dislocation segment experiences due to carbon interaction. As the dislocation bows out to form a kink pair, the cusp becomes less prominent. As we reach the transition state, the dislocation image intersects the carbon position, to minimise energy.

The pathway corresponding to the highest enthalpy image, can be seen in figure 15. Looking along a direction, we see the path a dislocation takes in going between adjacent peierls valleys is asymmetric, as expected due to the strong binding of carbon.

These features agree very well with the line tension model in Itakura [21], focussing on the case of dislocations undergoing kink-pair formation in the presence of a single hydrogen atom.

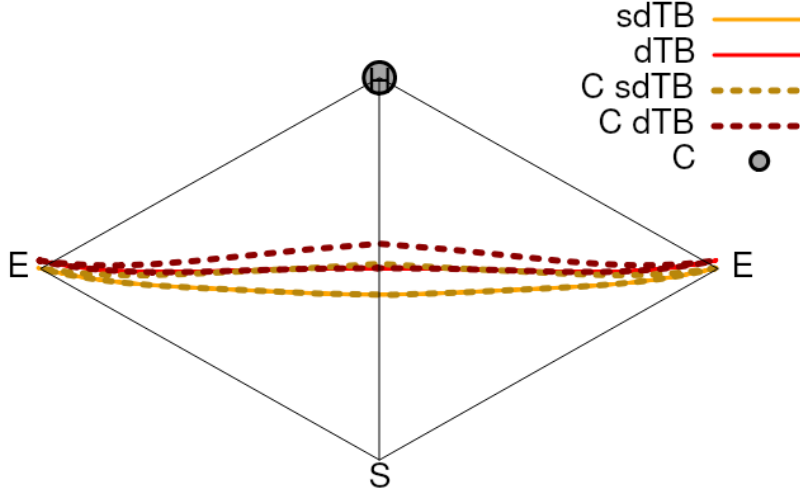


Figure 15: The migration path of the highest enthalpy images for both the *sd* and *d* tight-binding models with a single carbon in an E1 site. Carbon causes a deviation of the kink-pair formation path from the pure iron case (solid lines), due to carbon-dislocation binding.

The kink-pair formation enthalpy of *sd* and *d* iron models, in both pure iron, and with carbon ahead of the dislocation line are shown in figure 16. The shape agrees well with results of the line tension model of Itakura [22], and from atomistic calculations of EAM [49] and GAP [50] Fe potentials. We find that carbon produces a consistent reduction of  $\sim 25\text{meV}$  to the kink-pair formation enthalpy when placed ahead of the dislocation line. The reduction is surprisingly small compared to the effect of hydrogen interaction with dislocations [21], which gives a reduction of  $\sim 110\text{meV}$ . The discrepancy between carbon and hydrogen is due to the more gradual decrease of the carbon-dislocation interaction—over the distance between the initial and transition states—compared to the hydrogen-dislocation interaction, as shown in figure 11. Comparing the two interaction functions, we have at the peierls valley  $P_{\text{disl}} = (0,0)$ , and  $P^{\text{H}} = P^{\text{C}} = (1.17, 0.68)$  giving a distance  $d = 0.54b$  between the dislocation and the solute. The difference in the interaction energy for a dislocation segment in the final position in interaction for hydrogen  $\Delta E_b^{\text{H}} = E_b(\text{H}, 0) - E_b(\text{H}, 0.54b) = 150\text{ meV}$ , whereas for carbon we have  $\Delta E_b^{\text{C}} = E_b(\text{C}, 0) - E_b(\text{C}, 0.54b) = 40\text{ meV}$ .

Due to the longer range of the interaction function, we expect that a single carbon will provide comparable decreases to the kink-pair formation up to distances up to  $5b$ , if placed ahead of the dislocation line. At equilibrium, where carbon exhibits long-range ordering along the dislocation line in the H1 and H2 sites [41], we can expect

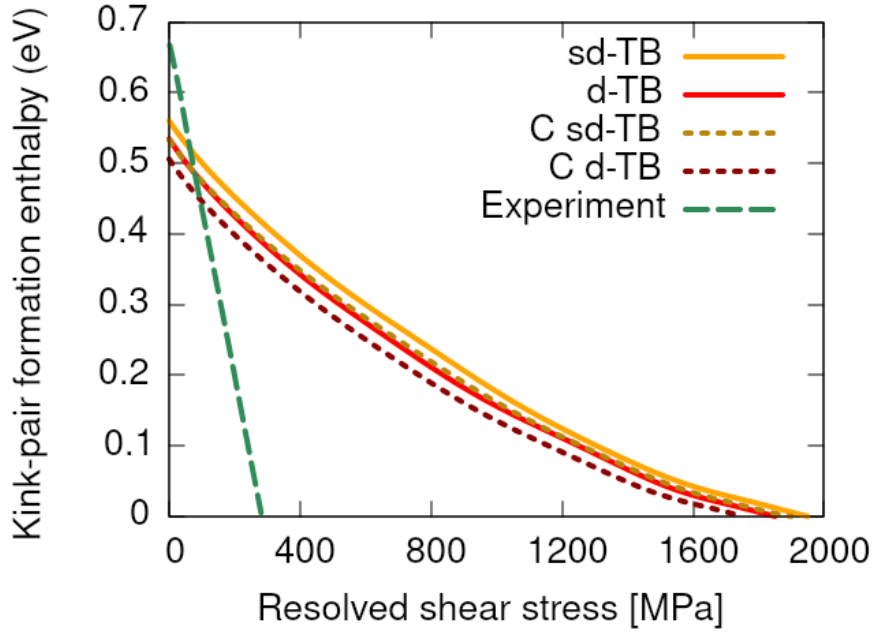


Figure 16: Dependence of the kink-pair formation enthalpy with increasing stress on the  $[111](\bar{1}\bar{1}0)$  direction. Solid lines: pure iron. Dotted lines: carbon ahead of the dislocation line in an octahedral site. Experimental data taken from Spitzig [48].

a decrease in the kink-pair formation enthalpy. Line-tension simulations in ordered carbon environments are necessary to account for this properly. We can approximately treat some of these effects using an effective carbon-dislocation interaction along the dislocation line during kink-pair formation, as shown in section 3.6.2.

The stress at which the kink-pair formation enthalpy becomes zero is the Peierls stress. In the zero temperature limit, we can approximately account for quantum effects, such as tunnelling and zero-point energy, by subtracting the Wigner correction, determined by quantum transition state theory [49, 51], from the kink-pair formation enthalpy. Calculating this correction within atomistic tight-binding simulations is currently intractable. The correction has been calculated using the Mendelev EAM potential [44] for a screw dislocation undergoing kink-pair nucleation [49]. The Wigner correction obtained is 0.09eV. We find that the Peierls stress obtained for both the *sd* and *d* models is  $\approx 1.2$ GPa, see table 5.

Discrepancies in the kink-pair formation enthalpy compared to experimental measurements of Spitzig [48], can be attributed to multiple sources. In bcc metals, experimental measurements of the CRSS, which can be linked to the kink-pair formation enthalpy, are thought to measure the stress required to operate Frank-Read sources which have been blocked due to the back stress of generated screw dislocations [53]. As mixed dislocations bow out from the source, long screw segments form—due to the higher mobility of mixed/edge character segments compared to screw segments. Between the source and the screw dislocations, there are non-screw dislocations, stresses from which act in conjunction with applied stress to reduce the necessary CRSS by 2-3 times. As such the enthalpy barrier obtained from the experimental CRSS measurements of Spitzig, cannot be directly compared to the true kink-pair formation enthalpy necessary for a single screw dislocation to undergo thermally-activated movement.

Table 5: Peierls stress of screw dislocation taken from the line tension model with the effect of the correction to the Peierls stress from quantum effects, estimated by Provile [49]. DFT results are found from papers of Itakura and Krach [22, 52], where Itakura *et al.* used a DFT-derived line-tension model, and Kraych used DFT NEB calculations. \* corresponds to use of Itakura DFT data in this implementation of the line-tension model.

Model	Peierls Stress [GPa]	Peierls Stress with Wigner correction [GPa]
sd-TB	1.95	1.35
C sd-TB	1.90	1.30
d-TB	1.85	1.30
C sd-TB	1.75	1.20
DFT [Kraych, 2019]	2.00	
DFT [Itakura, 2012]	1.00 [*2.10]	

### 3.5.4 Kink-pair nucleation rate

One can use an Arrhenius law to calculate the attempt frequency of a process given an energy barrier  $E_{\text{barrier}}$  [54],

$$\nu(E_{\text{barrier}}, T) = \nu_0 \exp\left(-\frac{E_{\text{barrier}}}{k_B T}\right), \quad (5)$$

where  $\nu_0$  is an initial attempt frequency.

The kink-pair nucleation rate of a dislocation of length  $N_d$  burgers vectors is given as [21]:

$$\nu_d = \nu(H_k(\sigma), T) N_d, \quad (6)$$

where  $H_k(\sigma)$  is the kink-pair formation enthalpy. Experimental results of *in situ* straining of Fe from Caillard [55], enable calculation of the attempt frequency for stable kink-pairs: assuming  $b = 2\mu\text{m}$ ,  $T = 300\text{K}$  and an applied stress of 33MPa one obtains  $\nu_d = 81\text{s}^{-1}$ .

There will be an enhancement of the rate due to carbon occupying sites ahead of the dislocation. Given a concentration of carbon on the dislocation line,  $c_d$ , we have in the sites ahead, the rate enhancement factor is

$$f_r(c_d, \Delta H_k, T) = 1 + c_d W_k \{\exp(\Delta H_k / k_B T) - 1\}. \quad (7)$$

where  $\Delta H_k = H_k - H_k^C = 25\text{meV}$  and  $W_k \sim 10b$  is the kink-width. Assuming  $T = 300\text{K}$ , and assuming the concentration of carbon is  $c_d^{\text{E2}}$ , we obtain enhancement factors as shown in table 6.

These rate enhancements are an order of magnitude less compared to what one finds with hydrogen in iron [43], due to the small reduction to the kink-pair formation enthalpy with carbon. However, this only accounts for a the effect of a single carbon just ahead of the core. Complex ordering phenomena of carbon has been found along the screw dislocation in Fe, which could enhance the kink-nucleation rate [41]. Using models parameterised on *ab-initio* data give equilibrium concentrations of different carbon trap sites along the dislocation core, accounting for carbon-carbon repulsion. They predict H1 and H2-type sites in adjacent layers can have concentrations which are  $\sim 1.0$  and  $\sim 0.25$  respectively, when the nominal carbon concentration is 100 appm. The effect of

Table 6: Enhancement factors to the kink nucleation rate and corresponding critical temperatures.  $c_d$  was taken as the value reached from self-consistency at  $T=300\text{K}$ , at a dislocation density of  $\rho = 10^{15}$ , as seen in figure 9. Kink-pair nucleation rate enhancements steadily increase until concentrations at which all dislocations are decorated with carbon, in the cases of  $C_{\text{nom}} \geq 500$  appm. The critical temperatures are all well above operating temperature, so we can expect rate enhancements during operation.

$c_{\text{nom}}$ [appm]	$f_r$ , Rate Enhancement factor	$T_U$ [K]
10	4.4	745
100	7.9	1329
500	17.3	3043
1000	17.3	3043

multiple carbon-dislocation interactions on the the kink-pair formation enthalpy has yet to be determined, but we expect  $\Delta H_k$  and therefore the rate enhancement, to increase.

Significant enhancement of the nucleation rate occurs when the rate enhancement factor is on the order of  $f_r \sim 1$  or greater. Defining  $c_d^E = \frac{1}{W_k \{\exp(\Delta H_k/k_B T) - 1\}}$ , one can impose a condition when  $c_d^E > c_d$ , defining a critical temperature  $T_U$  after which these enhancements are not deemed important. See table 6. All the critical temperatures are found to be above operating temperature.

The diffusion coefficient of carbon in bcc Fe has been calculated in DFT as  $D_C = 1.44 \times 10^{-7} \text{m}^2 \text{s}^{-1}$ , which agrees well with experiment [56, 57]. The attempt frequency is related to the diffusion coefficient by  $\nu_0 = 6D_0/a^2$  [58], which gives the attempt frequency of carbon as  $\nu_C^0 = 1.0 \times 10^{13} \text{s}^{-1}$  [38]. The migration energy barrier of carbon in bcc Fe was found to be  $E_C^{\text{m bulk}} = 0.87 \text{eV}$  in DFT calculations.

From the experimental rate of stable kink-pair nucleation  $\nu_d = 88 \text{s}^{-1}$  from Caillard, we can estimate the prefactor  $\nu_d^0 = 0.99 \times 10^8 \text{s}^{-1}$  using experimental the kink-pair formation enthalpy at 33 MPa [21].

The average velocity associated with a process undergoing thermal activation of a barrier is given by  $\bar{v} = d_{\text{barrier}} \nu$ , where  $d_{\text{barrier}}$  is the distance between the the initial and final states of the barrier. For dislocations we use  $d_d = a\sqrt{2/3}$  is the distance between Peierls valleys for kink-pair formation and  $d_C = 1.2$  is the distance between octahedral sites which carbon can jump to. As these distances are on the same order of magnitude, we omit the explicit calculation of velocities for clarity, using the attempt frequencies for comparisons.

At  $T = 300\text{K}$  and  $C_{\text{nom}} = 1000 \text{appm}$ , around the solubility limit of carbon in ferrite (0.02 wt% C), we have  $\nu_C(E_C^{\text{m bulk}}, 300) = 2.4 \times 10^{-2} \text{s}^{-1}$ , with  $f_r(1000 \text{appm}) \nu_d(H_k, 300) = 1.7 \times 10^{-1} \text{s}^{-1}$ . This shows that in the bulk, carbon cannot be assumed to move with the dislocation, as the attempt frequency of carbon is an order of magnitude less than that of kink-pair formation.

However, it has been shown in EAM calculations that much lower carbon migration barriers exist in the vicinity of a screw dislocations [38]. The migration barrier of carbon is reduced to  $E_C^{\text{m disl.}} = 0.2 \text{eV}$ . Using this value we obtain  $\nu_C(E_C^{\text{m disl.}}, 300) = 4.4 \times 10^9 \text{s}^{-1}$ . We see that the average carbon velocity will be much greater than that of dislocations undergoing thermally-activated movement, as such we can assume that in the high-mobility zone, that carbon is able to move with dislocations.

The timescale of carbon redistribution with dislocation movement remains negligible as long as the kink-pair formation enthalpy with carbon  $H_k^C(\sigma)$  is greater than the

migration barrier energy in high mobility zone:  $H_k(\sigma) - \Delta H_k^C(\sigma) > E_C^m$ . Using this value, we can obtain an upper critical stress  $\sigma_c^U \sim 210\text{MPa}$ , above which carbon cannot enhance dislocation mobility, as it cannot catch up with the dislocation.

### 3.5.5 Kink-trapping

Kink-trapping is the energetic barrier to kink-migration along the dislocation line due to the change in binding energy of a kink sweeping past a defect. The kink-trapping effect due to carbon can be estimated as follows [21]. If a kink-pair were to form with a carbon in an E1 site behind the dislocation, the carbon-dislocation binding energy will change. We can assume carbon remains in its site upon movement: the barrier to kink-migration has been shown to be small [21, 43, 35], as such kink-migration is orders of magnitude faster than that of carbon diffusion.

As the kink sweeps past, the E1 site becomes an E6 site, resulting in a difference in binding energy of  $\Delta E_b^{E1 \rightarrow E6} = 0.775 - 0.603 = 172\text{ meV}$ . This trapping effect is expected to decrease with applied stress, as shown in Itakura, but this is left for future work.

The kink-trapping effect of carbon will be pronounced when a dislocation moves from its equilibrium position as there will be multiple carbons along the dislocation line [41]. This effect has yet to be estimated.

This is an important effect to account for, as solute drag has been shown to reduce the kink-migration velocity sufficiently such that jogs can form on dislocations due to the collision of kinks on different glide planes causing pinning and the formation of edge dipoles seen in experiment [35, 59].

## 3.6 Line-tension equilibrium conditions

### 3.6.1 Dynamics of straight $1/2\langle 111 \rangle$ screw dislocation

Figure 17 shows the potential a straight screw dislocation experiences as it moves between Peierls valleys in an equilibrium carbon environment, allowing carbon to redistribute between trap sites upon glide. The potential a dislocation experiences decreases as carbon concentration is increased. This is due to the stabilisation of the hard core position with increases in carbon content. With stabilisation, E1/2 sites are distorted into H1 sites. At concentrations 20appm, the mean carbon-dislocation interaction energy becomes greater in magnitude than the bare Peierls potential, resulting in a potential well.

Figure 18 shows the case where the concentration of carbon is not allowed to equilibrate: simulating the limit of rapid glide, where the occupancies of carbon in all trap sites is fixed to the value determined at the initial easy-core configuration of the straight dislocation. The occupancies decrease rapidly with distance from the core. As such, the energy a straight dislocation experiences, relative to the initial dislocation position, increases with distance from the Peierls valley, due to a reduction in the dislocation-carbon interaction energy from a lack of carbon occupancy.

In reality, we have a situation which is between the two. This can be accounted for by a continuity term which is dependent on dislocation velocity [35].

### 3.6.2 Dynamics of kink-pair formation in equilibrium

The line-tension upon kink-pair formation, in the limit of slow glide, can be seen in figure 19. As the hard core is stabilised with increasing carbon content, the line tension

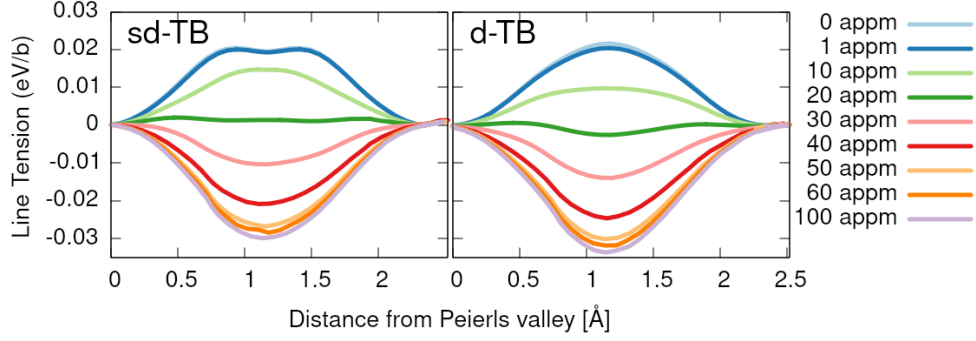


Figure 17: Enthalpies of straight screw dislocation in the line-tension model in an environment of carbon with concentrations determined by thermodynamical mean field model. Carbon concentration on the dislocation on the dislocation line is in equilibrium with the bulk according to the concentration given by the H1 site, where carbon is able to redistribute between the sites according to Maxwell-Boltzmann statistics.

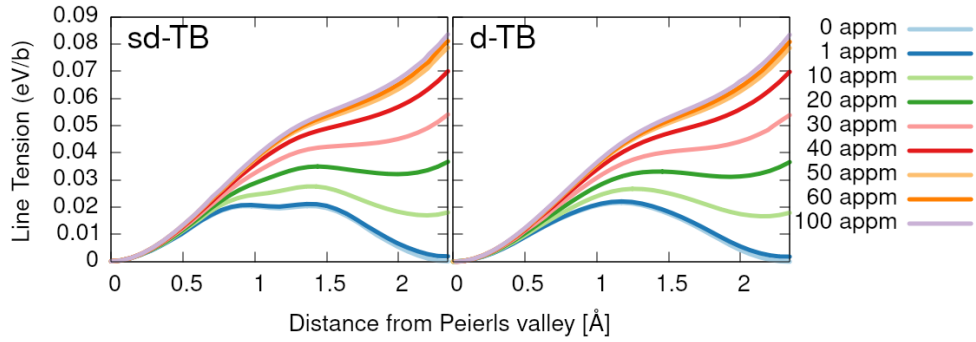


Figure 18: Enthalpies of straight screw dislocation in the line-tension model in an environment of carbon with concentrations determined by thermodynamical mean field model. Concentration of carbon in each of the sites is fixed to its initial value, simulating the limit where carbon does not have time to equilibrate with dislocation movement.

decreases, due to the negation of the bare Peierls potential with increasing carbon-dislocation interaction energy. At nominal concentrations greater than 20 appm, the string method finds lower energy dislocation configurations away from the straight initial easy core position favoured at lower concentrations.

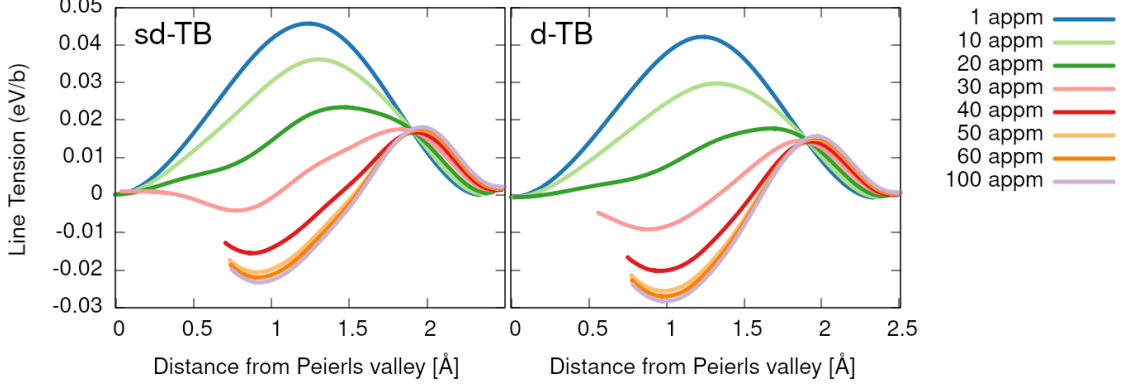


Figure 19: Enthalpies of the maximum enthalpy images upon kink-pair formation with increasing carbon content. Carbon interaction causes a reduction in the enthalpy barrier as due to the negation of the effect of the bare Peierls potential. As the nominal carbon concentration passes 20 appm, the hard core is stabilised, thus causing the string method algorithm to find a global minimum closer to the hard core position.

With increasing carbon concentration, both tight-binding models exhibit a deviation of the maximum enthalpy pathway towards the hard core, as shown in figure 20. At each concentration, the path a dislocation takes in the  $d$  tight-binding model is closer to the hard core, due to the morphology of its peierls potential.

The lineshapes of the  $P_x$  dislocation coordinate on kink-pair formation broaden with carbon content due to the attraction of the dislocation line to carbon sites.

The kink-pair formation enthalpy in an effective carbon concentration can be seen to decrease with increasing carbon content. At concentrations greater than 20 appm, the hard core is stabilised. Line-tension calculations of the kink-pair formation of a dislocation moving from the stabilised hard core to an adjacent hard-core position are necessary to ascertain the kink-pair formation enthalpy at higher carbon contents. We expect, as was seen in self-consistent calculations of the kink-pair formation enthalpy in hydrogen, that the trend will be reversed: the kink-pair formation enthalpy will increase with carbon content, once the hard core has been stabilised.

One can see the effect that these mean enthalpies have on the kink-pair nucleation rate. Using the results of the kink-pair formation enthalpy from the canonical- $d$  tight-binding model, and using equations (6) and (5) we have the rates as shown in table 7. The rate enhancement factor is not included here as the concentration term is taken into account in the kink-pair formation calculation itself.

Table 7: Kink-pair nucleation rate in an environment of carbon using the results of the canonical  $d$ -band model, using from equations (6) and (5)

$c_{\text{nom}}$ [appm]	$\nu^d$
10	8.7
20	2881.8

Allowing carbon to equilibrate between trap sites during kink-pair formation, we see



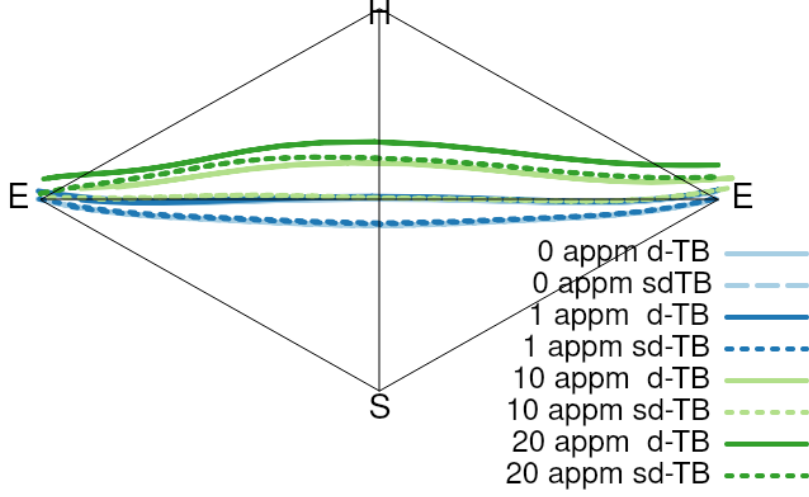


Figure 20: Maximum enthalpy pathways found upon kink-pair formation in an environment of carbon for both tight-binding models at different nominal carbon concentrations. Concentrations shown are before the easy core becomes unstable. With an increase in carbon content, path starts to deviate towards the hard core.

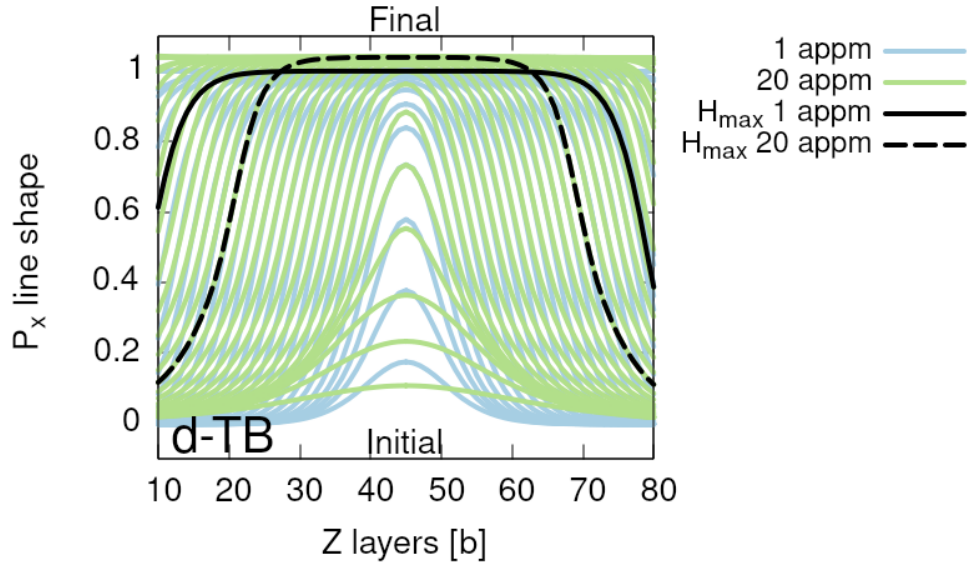


Figure 21:  $P_x$  lineshape comparison of differing concentrations of the canonical- $d$  tight-binding model.

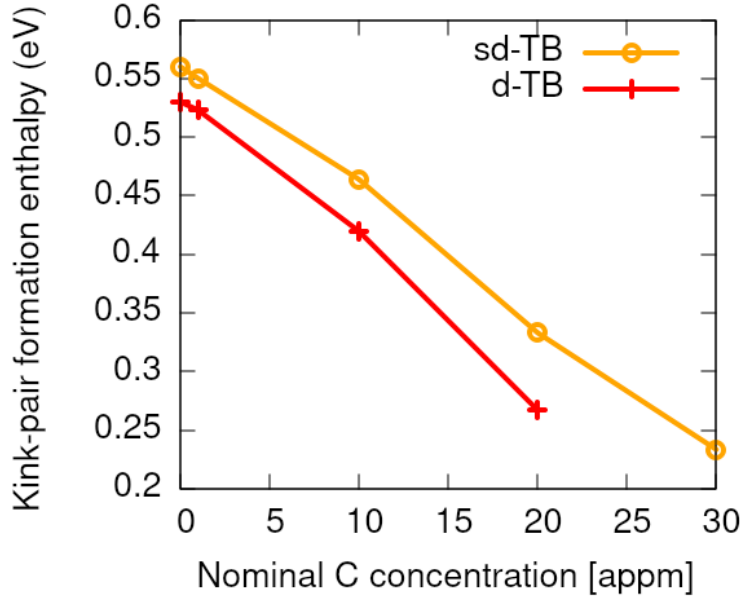


Figure 22: Kink-pair formation enthalpy dependence on nominal carbon concentration without the application of stress. There is a consistent decrease in the mean kink-pair formation enthalpy with carbon content.

a large enhancement to the kink pair nucleation rate, increasing dislocation velocity. Carbon remains with screw dislocations upon movement, due to the low barrier to migration in the high-mobility zone resulting in a velocity orders of magnitude greater than that of dislocation motion. The analysis shown here is approximate. A more complete description necessitates a self-consistent treatment of the kink-pair formation enthalpies, as  $H_k = H_k(\bar{v}_d)$  and  $\bar{v}_d = \bar{v}_d(H_k)$ . This is left for future work.

### 3.7 Diffusion Barriers

The diffusion barriers of carbon close to the easy core have been found to decrease—for some transitions—from 0.87eV for bulk diffusion, down to barriers around 0.2eV [38]. In the calculations shown in section 3.5.4, we see that carbon is able to keep up with the dislocation in a range of moderate velocities only if this diffusion barrier is lowered to such a level.

However, the predictive power of the EAM potential used to obtain these barriers is limited. The Mendelev EAM potential used in these calculations is unable to reproduce: the 2D Peierls potential, which is double-humped, instead of single-humped [44]; the metastable hard core structure, which exhibits a spontaneous reconstruction to the hard core from the easy core and, the binding energies of carbon close to the dislocation core—being roughly half that found in Ventelon and this work [46, 20]. These discrepancies are likely due to the inherent lack of quantum mechanics in EAM description of bonding, which seems necessary for an accurate description of energetics close to the dislocation core. As such, it remains to be seen if the diffusion barriers, and consequent diffusion rates obtained from this EAM potential are faithful.

As seen in figure 9, at moderate dislocation densities, we expect all dislocations to be decorated with carbon, and be of hard-core type. As such, it is important to ascertain

the diffusion barriers of carbon around the hard core, as it is the core we expect to find most commonly in iron. From this, we can ascertain if there exists a high-mobility zone around dislocations in bcc iron, validating the EAM results of Nematollahi and the Fe-C potential of Becquart [38, 46].

### 3.7.1 Theory

Using the diffusion barriers, we can find useful quantities, such as diffusion coefficients for each of the carbon sites around the hard core of the dislocation.

We follow the method detailed in the calculations of Lu *et al.* [60]. The diffusion coefficient is given by

$$D = D_0 \exp(-E_a/kT)$$

where  $D_0$  is a prefactor, and  $E_a$  is the activation energy. This can also be equivalently expressed as

$$D = n\beta d^2\Gamma,$$

where  $n$  is the number of nearest neighbour stable sites for the diffusing atom,  $\beta$  is the jump probability in the direction of diffusion,  $d$  is the length of the jump directed in the direction of diffusion and  $\Gamma$  is the jump rate between adjacent sites of the diffusing atom.

The jump rate is given by the equation,

$$\Gamma = \frac{kT}{h} \frac{\prod_{i=1}^{3N-6} [1 - \exp(-h\nu_i^0/kT)]}{\prod_{i=1}^{3N-7} [1 - \exp(-h\nu_i^*/kT)]} \exp(-\Delta H_m/kT)$$

Where we have the  $i^{\text{th}}$  normal mode frequency of the initial and saddle point images as  $\nu_i^0$  and  $\nu_i^*$ , respectively, where  $\Delta H_m$  is the difference in enthalpies between the saddle point and the initial image.

Can alternatively find  $\Gamma$  by obtaining the phonon free energy of a given image,

$$F_{\text{vib}} = kT \int_0^\infty g(\nu) \ln \left[ 2 \sinh \left( \frac{h\nu}{kT} \right) \right] d\nu$$

and so the jump rate can be expressed as

$$\Gamma = \frac{kT}{h} \exp[-(\Delta F_{\text{vib}} + \Delta H_m)/kT]$$

The zero point energy is included in the vibrational term.

Included in this is the assumption that using the harmonic approximation is valid throughout this. However for accurate elucidation of effects at finite temperature, anharmonicity must be included.

### 3.7.2 Computational Method

Elucidation of the diffusion barriers of carbon, was achieved using the Climbing-Image Nudged Elastic Band (CI-NEB) method with either 5 or 9 images. Fully-relaxed cluster simulation cells of dislocation-carbon interactions, as detailed above, were used for the initial and final images. Intermediate images were initially determined by a linear interpolation between the two. The same k-point mesh,  $1 \times 1 \times 12$  was used. The images

were relaxed until all forces were below  $20 \text{ meV}^{-1}$ . To prevent rotations and translations [61], six degrees of freedom were fixed for each image. The CI-NEB algorithm allows for the highest energy image to climb, by simply neglecting the spring forces acting on the image. This gives the true saddle point. Restoring forces were checked for each of the highest energy images.

The difference in vibrational free energies between cells comes from the difference in carbon placement from the initial images. One expects only significant changes the force constants calculated from the displacement of an atom close to the carbon defect. This implies that a good approximation to the true phonon free energy difference can be calculated using a subset of the original cell. This would further decrease the computational time necessary to obtain the vibrational free energy.

To facilitate the vibrational free energy calculations, we use the **phonopy** package [62]. With the addition of the defect in the cell, there is no symmetry to reduce the computational cost. This necessitates the displacement of each atom three times, for each degree of freedom. To reduce the computational cost, we allow **phonopy** to generate displacements from a smaller cell of radius  $R = 3\sqrt{2}a_{\text{bcc}}$ , cut out from the dynamic region. We assume here that the extra vibrational modes which arise from the omitted part of the computational cell will have a negligible effect on the difference in free energies, and thus the jump rate. The displacements generated are applied to the original cell and a calculation of the forces, under self-consistency to a charge tolerance of  $1e-6$ , is performed. The forces acting on particular atoms are extracted and fed into phonopy, from which we obtain the vibrational free energy.

### 3.7.3 Enthalpies in dislocation movement with static carbon

We can find the change in Gibbs free energy of a dislocation as it moves from one configuration to another. If the difference between configurations is less than zero, we can regard the change as favourable for the system. Assuming the whole dislocation line moves at at once, carbon remains in its original binding position, and neglecting the energy difference arising from the slightly different elastic dipole tensors generated from the different environments of carbon around each core, from equation 2.5 we have

$$\Delta H_{\text{LT}} = \Delta H_{\text{core 1} + \text{C}\alpha \rightarrow \text{core 2} + \text{C}\beta} = \Delta E_{\text{core}}^{1 \rightarrow 2} + (\sigma \cdot \vec{b}) \times \vec{l} \cdot (\Delta \vec{P}_{\text{core}}) - \Delta E_{\text{b}}^{\text{C}\alpha \rightarrow \text{C}\beta} \quad (8)$$

The change in the Gibbs free energy is given by  $\Delta G(T, \sigma) = \Delta H(\sigma) - T\Delta S = \Delta H_{\text{LT}}(\sigma) + \Delta F_{\text{vib}}(T, V) + \Delta F_{\text{conf}}(T, V)$ , ignoring electronic and magnetic contributions and assuming constant volume, where  $H_{\text{LT}}$  is the enthalpy of the line tension model.

The vibrational contribution to the free energy can be obtained by calculation of the phonon density of states, as done by calculations by **phonopy**. Considering only those binding sites sampled close to the core, there are up to six equivalent sites for carbon around the core, due to the three-fold rotational symmetry about the dislocation core in addition to three  $C_2$  point groups with rotation axes at 30 deg, 90 deg and 120 deg, as measured from the  $x$ -axis, as seen in figure 8. The configurational entropy therefore has a maximum magnitude of  $S_{\text{conf}} = k_{\text{b}} \ln(\Omega) = k_{\text{B}} \ln(6)$ , as such we can say the change in configurational entropy is negligible, due to the magnitude of the Boltzmann constant. Therefore we obtain

$$\Delta G = \Delta E_{\text{core}}^{1 \rightarrow 2} - \Delta E_{\text{b}}^{\text{C}\alpha \rightarrow \text{C}\beta} + \Delta F_{\text{vib}} + (\sigma \cdot \vec{b}) \times \vec{l} \cdot (\Delta \vec{P}_{\text{core}}) \quad (9)$$

In going from the hard core to the easy core, we have:

$$\Delta G_{\text{d. hard} + \text{C}\alpha \rightarrow \text{d. easy} + \text{C}\beta} = -\Delta E_{\text{core}}^{\text{Easy-Hard}} + (\sigma \cdot \vec{b}) \times \vec{l} \cdot (\vec{P}_{\text{hard}} - \vec{P}_{\text{easy}}) - \Delta E_{\text{b}}^{\text{H}\alpha \rightarrow \text{E}\beta} \quad (10)$$

$$= -40\text{meV} - \sigma_{yz} \cdot \frac{\sqrt{3}}{2} a_{\text{bcc}} + \Delta F_{\text{vib}} - \Delta E_{\text{b}}^{\text{H}\alpha \rightarrow \text{E}\beta} \quad (11)$$

$$\therefore \quad \text{if} \quad \Delta F_{\text{vib}} < 40\text{meV} + \sigma_{yz} \cdot \frac{\sqrt{3}}{2} a_{\text{bcc}} + \Delta E_{\text{b}}^{\text{H}\alpha \rightarrow \text{E}\beta}$$

then the change is favourable.

at zero stress, we have

$$\Delta E_{\text{core 1} + \text{C}\alpha \rightarrow \text{core 2} + \text{C}\beta} = \Delta E_{\text{core}}^{1 \rightarrow 2} - \Delta E_{\text{b}}^{\text{C}\alpha \rightarrow \text{C}\beta} \quad (12)$$

where, core 1/core 2 are easy/hard dislocations, C $\alpha$ / $\beta$  are labels for the binding site of the carbon relative to core 1/core 2,  $\Delta E_{\text{core}}^{1 \rightarrow 2}$  is the energy necessary to transform between core 1 to core 2 (difference in peierls potential of the cores) and  $\Delta E_{\text{b}}^{\text{C}\alpha \rightarrow \text{C}\beta}$  is the

difference in binding energy of carbon between the two cores. If this energy change,  $\Delta E_{\text{core 1} + \text{C}\alpha \rightarrow \text{core 2} + \text{C}\beta}$  is negative, then one can assume that this is a favourable process, and the difference in enthalpy is available for the activation of a diffusion barrier. We can think of the second term, as the work done by the dislocation against the external stress field to move to an adjacent core position. In general, the stress tensor used should incorporate the stress due to the tetragonal distortion of the carbon as well as applied stress. We do not incorporate this effect in this analysis.

#### 3.7.4 Modification of occupancies due to diffusion barrier

To model the solute atmosphere around a dislocation in an environment of carbon, which is allowed to diffuse, we can use a discrete diffusion model, as detailed in Yoshinaga [63]. Applying harmonic transition-state theory to the migration of carbon to adjacent sites around each of the cores, we are able to ascertain the energy barriers, and therefore the rates of carbon diffusion around each of the cores, from which we can determine the evolution of carbon concentration with time. Nematollahi *et al.* [38] extended this model to include the effect of changes in occupancy upon dislocation movement.

The total change in occupancy can be described by the equation

$$\begin{aligned} \frac{\partial \chi_i}{\partial t} = \sum_{j=1}^4 \left\{ \chi_j (1 - \chi_i) \nu_0^{\text{migration}} \exp \left[ -E_{\text{barrier}}^{i \rightarrow j} / k_B T \right] \right. \\ \left. - \chi_i (1 - \chi_j) \nu_0^{\text{migration}} \exp \left[ -E_{\text{barrier}}^{j \rightarrow i} / k_B T \right] \right\} + \frac{\bar{v}_{\text{disl}}}{a/2} [\chi_{j+} - \chi_i], \end{aligned}$$

where  $\chi_i$ , is the occupancy of a particular carbon site,  $E_{\text{barrier}}^{j \rightarrow i}$ , is the migration barrier of carbon from site  $j$  to site  $i$ ,  $\nu_0$  is the attempt frequency. The summation is over the four nearest sites available for carbon to diffuse to. The last term in equation (??), is a convection term, allowing concentrations to change upon a dislocation moving with average velocity  $\bar{v}_{\text{disl}}$ . We use the convention of a dislocation moving along the positive

axis; as such,  $\chi_{j+}$  is the occupation of a site to the right of site  $i$  the dislocation, which is biased to move towards the  $\chi_i$  upon dislocation movement, and similarly site  $i$  will move the the  $j-$  site, to the left of the dislocation.

In the paper of Gong *et al.* [35], the diffusion model has a different form. The occupancy of carbon is taken as a proportion of the difference between the limiting cases of dislocation movement: slow dislocation movement, where carbon is able to equilibrate with the dislocation, and fast dislocation movement, where carbon occupancies are fixed. This has the form of

$$\frac{\partial \chi_i}{\partial t} = \bar{v}_{\text{disl}} \frac{\partial \chi_i}{\partial x} = (\chi_i^e(x) - \chi_i(x, \bar{v})) \nu_0^{\text{solute escape}} \exp -E_i(r)/k_B T,$$

where  $\chi_i^e$  is the equilibrium occupancy of site  $i$ ,  $\chi_i$  is the true occupancy of the site, which is solved for,  $\nu_0^{\text{solute escape}}$  is the attempt frequency for carbon to escape the solute atmosphere, and  $E_i(r)$  is the *binding* energy of carbon to the  $i^{\text{th}}$  site, which has been parameterised by a dependence on the distance from the dislocation core  $r$ . This equation can be solved self-consistently with

$$\bar{v}_{\text{disl}}(E_{\text{KP}}) = h \nu_{\text{KP}}^0 \exp(-E_{\text{KP}}(C_C, \sigma, \bar{v}_{\text{disl}})),$$

where  $h = a\sqrt{2/3}$  is the distance between two Peierls valleys,  $\nu_{\text{KP}}^0 = 2.31 \times 10^9 \text{s}^{-1}$  is the attempt frequency for stable kink-pair formation and  $E_{\text{KP}}$  is the kink-pair formation enthalpy at a given carbon concentration, stress and average dislocation velocity.

- In Ivo's paper, the change in occupancy has a time dependence, which is due to the velocity of a dislocation.
- This mediated between the two limiting regimes of static and equilibrium occupancies upon dislocation motion.

$$\frac{\partial \chi_i}{\partial t} = \bar{v} \frac{\partial \chi_i}{\partial x} = (\chi_i^e(x) - \chi_i(x, \bar{v})) \nu_0^{\text{solute escape}} \exp -E_i(r)/k_B T$$

- Here the attempt frequencies are different as one is for a hydrogen to escape from the binding of the dislocation to the bulk, and the other is to escape the relative energy barrier between sites.
- If it is possible to assume that one can superimpose the occupancy effects of carbon diffusion, then we can have an equation for the velocity dependence.

## 4 Discussion

The Peierls potential is reproduced well by tight-binding. For a Peierls potential more reminiscent of finite temperature materials, one could have given a more thorough treatment of magnetism. All calculations were performed at 0 K, using the ferromagnetic ground state of iron during dislocation relaxations. One could have performed multiple dislocation relaxations using the noncollinear disordered local moment approximation to handle paramagnetism, as was achieved by Casillas and Ventelon [64]. Their calculations showed that the energy difference between the hard and easy cores is lowered to  $26 \pm 20 \text{meV}/b$ , from  $40 \text{meV}/b$ . The error bars are too large to confirm the hypothesis that the Peierls potential is significantly different, and the tight-binding results coincidentally fall exactly into the middle of their range. As such, the resultant Peierls

potential from ferromagnetic calculations within tight-binding was deemed suitable for the line-tension model.

We see a reduction in the kink-pair formation enthalpy of pure iron in tight-binding, by 0.15eV compared to DFT, due to the smaller overall Peierls potential in both the *sd* and *d* tight-binding models. This would increase the rate of kink nucleation in kMC models, causing a higher overall dislocation velocity. We do not expect this discrepancy will significantly change the principal mechanisms observed, or results obtained, from kMC simulations.

As in Lüthi [65], carbon interactions were found to be vital in understanding how screw dislocations move in steels, due to the spontaneous reconstruction of the pure iron ground state (easy core) upon introduction of carbon. From the large binding energy of the H1 site, one would expect a hard core with carbon in a prismatic site as the ground state configuration for pinned dislocations.

In the context of dislocation-assisted carbon migration, with sufficient contact stress, dislocations in their hard core ground state will be forced to move (say, along the  $X = \langle 211 \rangle$  direction), which results in the hard core reconstructing to an easy core. In the limit of rapid glide, the prismatic carbon will stay in-place, becoming an E1 site. A drag force now acts to impede motion of the dislocation, due to the binding of the carbon in the E1 site. Progression of dislocation glide results in further reconstruction of the dislocation core to hard and easy states, with the original carbon being situated in H2, E6 and H3 sites, relative to the dislocation centre. Thus as the dislocation moves, there is a significant drag force acting on the dislocation, which decreases the further the dislocation moves from carbon, as one would expect. In this scenario, the kink-pair formation would increase greatly, due to this drag force. However, due to the reduced barrier for carbon migration within the vicinity of a dislocation and large average velocity in comparison to the screw dislocation, we cannot assume that carbon will stay in-place. These results suggest a dislocation-assisted carbon migration mechanism could be feasible, but the last stage of the multi-scale model, SCkMC, is necessary to verify this.

In normal operating temperatures of the bearing, one expects all dislocations to be hard cores saturated with carbon in most of the H $j$  sites, as seen in the concentration analysis. In ferrite that has just transformed, assuming a C concentration of 0.6 wt% as seen in martensite, we expect similar behaviour to the 1000 appm case as seen in figure 9.

## 5 Future work

Using the kink-pair formation enthalpies and the binding energies of carbon to screw dislocations, one can proceed with self-consistent kinetic Monte Carlo simulations of dislocation glide in an environment of carbon to understand how dislocations move carbon under applied stress, in different temperature and nominal carbon concentration regimes.

It would be of interest to pursue atomistic calculations of carbon bound to edge dislocations. Recent DFT/Eshelby theory calculations by Maugis *et al.* [66], show under *compressive* stress, carbon diffusivity is *enhanced*. Pipe diffusion along edge dislocations could therefore be an important aspect to consider in carbon transport, in addition to the higher mobility of edge dislocations in bcc iron. As such, edge dislocations could be quite important within the mechanism of dislocation-assisted carbon migration.

Ising and Monte Carlo models of intersite carbon interactions have been performed using the results of DFT carbon-dislocation binding energies [65]. These calculations

only considered the hard core, with carbon binding sites of the H1 prismatic site and a H2 site, (which they name  $P$  and  $O^{(4)}$  respectively). First neighbour C-C interactions were taken into account, both along the dislocation line and between carbon sites. Using the tight-binding calculations detailed in this report, we can easily apply and extend this analysis to consider more binding sites around the hard core, and observe stable carbon distributions around the easy core. Furthermore, we could calculate the kink-pair formation enthalpy in an environment of multiple carbons, accounting for the long-range ordering exhibited by carbon explicitly.

Analysis of carbon diffusion barriers around a dislocation are crucial to determining the regimes in which dislocation-assisted carbon migration is valid. EAM calculations by Nematollahi [38], find carbon migration energy barriers are significantly reduced around dislocations, giving rise to a "high mobility zone". Measurement of the migration barriers (and diffusion coefficient) for carbon to move to different sites around a screw dislocation has not been achieved with a quantum-mechanical interatomic force method, such as tight-binding, and could provide more accurate estimations of the average carbon velocity, critical stresses and critical temperatures above which carbon cannot catch up with dislocations—a crucial part of the theory of dislocation-assisted carbon migration. Future work will be to measure this diffusion barrier to determine if there are significant modifications to the kink-pair nucleation rate.

## 6 Conclusion

Dislocation-assisted carbon migration is thought to be a viable mechanism by which martensite decays to form DER regions—mostly composed of ferrite interspersed in a martensitic matrix—which enhances failure risk by RCF. There is dispute over where excess carbon from the martensitic matrix finds itself upon transformation to ferrite, of much lower carbon solubility. The current leading mechanism suggests carbon segregates to pre-existing carbides, yet experimental results show in the late stages of DER formation, pre-existing carbides are partially dissolved in areas of highly localized plasticity, implying segregation of carbon to dislocations. As such, a thorough investigation of carbon-dislocation interactions is vital to understanding how DER initially forms and progresses.

Atomistic calculations using tight-binding, the first stage in a multi-scale paradigm to understand dislocation-assisted carbon migration, found a Peierls potential with characteristics comparable to both EAM/DFT results.

Carbon distribution around the easy and hard cores were found to differ significantly, with the largest binding energy being found by carbon being situated in a prismatic site in the hard core. Carbon within 3Å of the easy core caused reconstruction to the hard core, with carbon in a prismatic site.

Equilibrium concentrations of carbon around the hard/easy cores at normal operating temperatures suggest that all dislocations are of hard core type with carbon situated in a H1/prismatic site, with reconstruction of all easy core dislocations to hard core, resulting in all dislocations being pinned.

If a dislocation moves under stress from the hard core-prismatic carbon ground state, a large drag force acts on the dislocation upon movement to adjacent easy and hard positions, assuming the carbon will stay in place due to its low diffusion coefficient, relative to dislocation velocity. The carbon-dislocation binding energies decrease with distance, and are in good agreement with literature. This suggests that a dislocation-



assisted carbon migration mechanism is plausible, but more work needs to be done to confirm if so.

Calculations of the kink-pair formation enthalpy using a line-tension model finds a single carbon to have a surprisingly subtle effect on the kink-pair formation enthalpy. Allowing carbon to equilibrate between trap sites, we see the average kink-pair formation enthalpy decreases significantly upon stabilisation of the hard core. A self-consistent method is necessary to obtain more accurate estimates of the kink-pair formation enthalpy and average dislocation velocity.

Further work will be done to ascertain diffusion barriers around the dislocation, which have been shown to be significantly reduced from bulk values due to the presence of dislocations in DFT/EAM calculations [38]. These migration energy barriers are crucial to the solute drag mechanism.

SCKMC simulations will be used to determine dislocation dynamics in an environment of carbon.

## 7 Appendix

### 7.1 Regularisation of interaction energy in quadrupolar array

In isotropic elasticity, the elastic energy of a single dislocation dipole in an infinite lattice is given by

$$E_{\text{el}}^{\infty} = \frac{\mu b^2}{4\pi} \ln \left( \frac{r}{r_c} \right)$$

The contribution from periodic images to the correction is

$$E_{\text{img}} = E_{\text{el}}(\mathbf{a}, \mathbf{c}_i, r_c) - E_{\text{el}}^{\infty}(\mathbf{a}, r_c),$$

"Ghost" dipoles are introduced to account for the conditional convergence of the sum at  $\pm\alpha\mathbf{b}$  and  $\pm\beta\mathbf{b}$ , where  $\alpha = \beta = 0.5$ . We define  $E_{\text{dg}}(\mathbf{R})$  as the interaction energy of a ghost dislocation and a dipole at  $\mathbf{R}$  anisotropic elasticity equations as shown in [67].

Defining,

$$E_{\text{dd}}(\mathbf{R}) = \frac{\mu b^2}{2\pi} \ln \frac{|\mathbf{R}|^2}{|\mathbf{R} + \mathbf{a}| \cdot |\mathbf{R} - \mathbf{a}|},$$

we obtain,

$$E_{\text{img}} = \frac{1}{2} \sum_{\mathbf{R}} [E_{\text{dd}}(\mathbf{R}) - E_{\text{dg}}(\mathbf{R})] - \frac{1}{2} E_{\text{dg}}(\mathbf{R} = 0),$$

which can be subtracted from the total energy as given from atomistic calculations, for a regularised interaction energy.

### 7.2 Zero-point energy calculation

After relaxation of the C-dislocation system, a 3x3 Hessian matrix is constructed by taking the numerical derivative of forces observed on the carbon atom after displacement by  $\pm 0.015$  in each of the  $X$ ,  $Y$  and  $Z$  directions. The three atoms surrounding the core on the first and third layers were again fixed in  $Z$  coordinate. The zero-point energy is given by

$$E_z = \frac{1}{2} \sum_{i=1}^3 \frac{h}{2\pi} \sqrt{k_i/m_C},$$

where  $k_i$  are the eigenvalues of the Hessian and  $m_C$  is the mass of carbon.

### 7.3 Smooth mapping of sites in equilibrium line-tension model

To approximate the position of trap sites upon dislocation movement, the  $x$ -coordinate of the dislocation core position,  $P_x$ , was used to obtain the trap site positions around the core.

Focussing on one half of the the path of a dislocation between peierls valleys, the segment of a dislocation going between an easy core to hard core, one can define forward and backwards paths, a dislocation travelling from the easy core towards the hard core, and vice versa. The trap sites at the end points are well-defined: when  $P_x = P_x^{\text{easy}} = 0$ , the trap sites are exactly those found upon relaxation of the easy core, similarly, when  $P_x = P_x^{\text{hard}} = a\sqrt{2}/(2\sqrt{3}) = d$ , the trap sites are those found upon relaxation of the hard core. These positions can be seen in section 3.3.

One can define trap site mappings for these forward and backwards paths: for an easy core site to a hard core site,  $E_j^\alpha \rightarrow H_k^\beta$ , and from hard core to easy core  $H_l^\gamma \rightarrow E_m^\delta$ , where  $j, k, l, m$  denote a particular trap site position, with labels defined in section 3.3 and  $\alpha, \beta, \gamma, \delta$  are labels which denote which of the six possible sectors the site belongs to. These six sectors arise from the combination of the three-fold rotational and reflection symmetry found in the crystal—thus one need only have the trap sites for one sector and apply the appropriate rotation and/or reflection to obtain the necessary trap site position at the given endpoint. These mappings are not symmetric for the forward and backwards paths, *e.g.* are many easy core trap sites which map to the H1 site, due to its strong binding energy, as found in atomistic simulations of reconstruction, but, quite clearly, these mappings

For a given mapping, one can linearly interpolate between the two positions to give a trap site position for an intermediate dislocation core.

$$P_{j,k}^{\text{trap forward}}(P_x) = \left(1 - \frac{P_x}{d}\right) E_j^\alpha + \frac{P_x}{d} H_k^\beta,$$

$$P_{l,m}^{\text{trap backward}}(P_x) = \left(1 - \frac{P_x}{d}\right) E_m^\delta + \frac{P_x}{d} H_l^\gamma.$$

To define trap site mappings for core positions at  $P_x > d$ , one need only swap the forward for the backwards path, due to reflection symmetry about  $P_x = d$ , thus allowing for well defined trap sites for all core positions between the peierls valleys. This can be seen in the kink-pair formation of the canonical- $d$  tight-binding model in figure 23.

## 8 Bibliography

### References

- [1] Steve Ooi, Junbiao Lai, Sebastián Restrepo, Rose Yan, and Erik Vegter. Dark etching regions under rolling contact fatigue: a review. page 20, 2019.

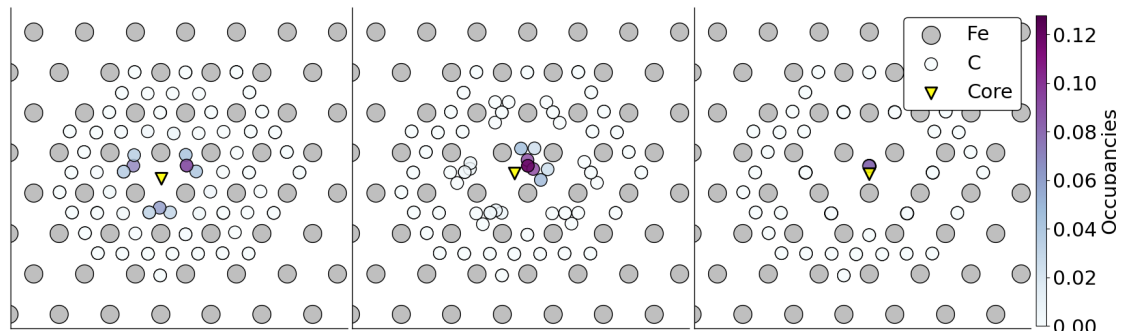


Figure 23: Positions of trap sites around dislocation segments upon kink-pair formation at a nominal carbon concentration of 30 apm. Path only shown to the hard core to demonstrate smooth mapping of trap sites going from easy to hard core. Equilibrium occupancies shown by coloured circles.

- [2] H. Fu, E.I. Galindo-Nava, and P.E.J. Rivera-Díaz del Castillo. Modelling and characterisation of stress-induced carbide precipitation in bearing steels under rolling contact fatigue. *Acta Materialia*, 128:176–187, April 2017.
- [3] A. H. King and J. L. O’Brian. *Microstructural Alterations in Rolling Contact Fatigue*, pages 74–74–15. Advances in Electron Metallography: Vol. 6. ASTM International, nil.
- [4] A. B. Jones. *Metallographic Observations of Ball Bearing Fatigue Phenomena*, pages 35–35–18. Symposium on Testing of Bearings. ASTM International, nil.
- [5] J. J. Bush, W. L. Grube, and G. H. Robinson. Microstructural, microhardness and residual stress changes due to rolling contact. *Tribology*, 3(4):249, 1970.
- [6] H. Swahn, P. C. Becker, and O. Vingsbo. Martensite decay during rolling contact fatigue in ball bearings. *Metallurgical Transactions A*, 7(8):1099–1110, August 1976.
- [7] AP Voskamp. Fatigue and material response in rolling contact. 1997.
- [8] A. P. Voskamp and E. J. Mittemeijer. State of residual stress induced by cyclic rolling contact loading. *Materials Science and Technology*, 13(5):430–438, 1997.
- [9] I Polonsky. On white etching band formation in rolling bearings. *Journal of the Mechanics and Physics of Solids*, 43(4):637–669, 1995.
- [10] Viktorija Smelova, Alexander Schwedt, Ling Wang, Walter Holweger, and Joachim Mayer. Electron microscopy investigations of microstructural alterations due to classical rolling contact fatigue (rcf) in martensitic aisi 52100 bearing steel. *International Journal of Fatigue*, 98(nil):142–154, 2017.
- [11] Ragnar Österlund and Olof Vingsbo. Phase changes in fatigued ball bearings. *Metallurgical Transactions A*, 11(5):701–707, May 1980.
- [12] N. Mitamura, H. Hidaka, and Setsuo Takaki. Microstructural development in bearing steel during rolling contact fatigue. *Materials Science Forum*, 539-543:4255–4260, Mar 2007.

- [13] Hanwei Fu, Wenwen Song, Enrique I. Galindo-Nava, and Pedro E.J. Rivera-Díaz del Castillo. Strain-induced martensite decay in bearing steels under rolling contact fatigue: Modelling and atomic-scale characterisation. *Acta Materialia*, 139(nil):163–173, 2017.
- [14] Anurag Warhadpande, Farshid Sadeghi, and Ryan D. Evans. Microstructural alterations in bearing steels under rolling contact fatigue part 1—historical overview. *Tribology Transactions*, 56(3):349–358, May 2013.
- [15] Anurag Warhadpande, Farshid Sadeghi, and Ryan D. Evans. Microstructural alterations in bearing steels under rolling contact fatigue: Part 2—diffusion-based modeling approach. *Tribology Transactions*, 57(1):66–76, November 2013.
- [16] A. P. Voskamp, R. Österlund, P. C. Becker, and O. Vingsbo. Gradual changes in residual stress and microstructure during contact fatigue in ball bearings. *Metals Technology*, 7(1):14–21, 1980.
- [17] S.H. Hashemi. Strength-hardness statistical correlation in api x65 steel. *Materials Science and Engineering: A*, 528(3):1648–1655, 2011.
- [18] H. K. D. H. Bhadeshia. Solution to the bagaryatskii and isaichev ferrite–cementite orientation relationship problem. *Materials Science and Technology*, 34(14):1666–1668, May 2018.
- [19] A. T. Paxton and C. Elsässer. Analysis of a carbon dimer bound to a vacancy in iron using density functional theory and a tight binding model. *Physical Review B*, 87(22), June 2013.
- [20] Lisa Ventelon, B. Lüthi, E. Clouet, L. Proville, B. Legrand, D. Rodney, and F. Willaime. Dislocation core reconstruction induced by carbon segregation in bcc iron. *Physical Review B*, 91(22), June 2015.
- [21] M. Itakura, H. Kaburaki, M. Yamaguchi, and T. Okita. The effect of hydrogen atoms on the screw dislocation mobility in bcc iron: a first-principles study. *Acta Materialia*, 61(18):6857–6867, 2013.
- [22] M. Itakura, H. Kaburaki, and M. Yamaguchi. First-principles study on the mobility of screw dislocations in bcc iron. *Acta Materialia*, 60(9):3698–3710, May 2012.
- [23] Emmanuel Clouet. Screw dislocation in zirconium: An ab initio study. *Physical Review B - Condensed Matter and Materials Physics*, 86(14):1–11, 2012.
- [24] Vasily Bulatov. *Computer Simulations of Dislocations (Oxford Series on Materials Modelling)*. Oxford University Press, dec 2006.
- [25] Emmanuel Clouet, Lisa Ventelon, and F. Willaime. Dislocation core energies and core fields from first principles. *Physical Review Letters*, 102(5), February 2009.
- [26] Peter M. Anderson, John Price Hirth, and Jens Lothe. *Theory of Dislocations*. Cambridge University Press, 2017 edition edition. Originally published: New York : McGraw-Hill, 1967. Editions published: New York : Wiley, 1982, and Malabar, FL : Krieger, 1992.

- [27] G. Tréglia, B. Legrand, F. Ducastelle, A. Saúl, C. Gallis, I. Meunier, C. Mottet, and A. Senhaji. Alloy surfaces: Segregation, reconstruction and phase transitions. 15(2):196–235.
- [28] D. McLean. *Grain Boundaries in Metals*. Monographs on the physics and chemistry of materials. Clarendon Press, 1957.
- [29] S. Morito, J. Nishikawa, and T. Maki. Dislocation density within lath martensite in fe-c and fe-ni alloys. *ISIJ International*, 43(9):1475–1477, 2003.
- [30] Oleg M. Braun and Yuri S. Kivshar. Nonlinear dynamics of the Frenkel–Kontorova model. 306(1):1–108.
- [31] T Kontorova and J Frenkel. On the theory of plastic deformation and twinning. II. *Zh. Eksp. Teor. Fiz.*, 8:1340–1348, 1938.
- [32] J Frenkel and T Kontorova. On the theory of plastic deformation and twinning. *Izv. Akad. Nauk, Ser. Fiz.*, 1:137–149, 1939.
- [33] David Rodney and Laurent Proville. Stress-dependent peierls potential: Influence on kink-pair activation. *Physical Review B*, 79(9), March 2009.
- [34] Stela Makri, Christoph Ortner, and James R. Kermode. A preconditioning scheme for minimum energy path finding methods. *The Journal of Chemical Physics*, 150(9):094109, March 2019.
- [35] Peng Gong, Ivaylo H. Katzarov, John Nutter, Anthony T. Paxton, and W. Mark Rainforth. The influence of hydrogen on plasticity in pure iron—theory and experiment. 10(1):10209.
- [36] A. H. Cottrell and B. A. Bilby. Dislocation Theory of Yielding and Strain Ageing of Iron. 62(1):49–62.
- [37] R G A Veiga, M Perez, C S Becquart, and C Domain. Atomistic modeling of carbon Cottrell atmospheres in bcc iron. 25(2):025401.
- [38] Gh. Ali Nematollahi, Blazej Grabowski, Dierk Raabe, and Jörg Neugebauer. Multi-scale description of carbon-supersaturated ferrite in severely drawn pearlitic wires. *Acta Materialia*, 111:321–334, June 2016.
- [39] R.G.A. Veiga, M. Perez, C.S. Becquart, E. Clouet, and C. Domain. Comparison of atomistic and elasticity approaches for carbon diffusion near line defects in -iron. *Acta Materialia*, 59(18):6963–6974, October 2011.
- [40] N. Louat. The Effect of Temperature on Cottrell Atmospheres. 69(4):459–467.
- [41] B Lüthi, F Berthier, L Ventelon, B Legrand, D Rodney, and F Willaime. *Ab Initio* thermodynamics of carbon segregation on dislocation cores in bcc iron. 27(7):074002.
- [42] E. R. M. Davidson, T. Daff, G. Csanyi, and M. W. Finnis. Grand canonical approach to modeling hydrogen trapping at vacancies in  $\alpha\text{-Fe}$ . 4(6):063804.

- [43] E. Simpson. *A Tight Binding Study of Dislocations in Iron and Their Interactions with Hydrogen*. PhD thesis, King’s College London, 2019.
- [44] M. I. Mendelev, S. Han, D. J. Srolovitz, G. J. Ackland, D. Y. Sun, and M. Asta. Development of new interatomic potentials appropriate for crystalline and liquid iron. *Philosophical Magazine*, 83(35):3977–3994, December 2003.
- [45] Emmanuel Clouet, Sébastien Garruchet, Hoang Nguyen, Michel Perez, and Charlotte S. Becquart. Dislocation interaction with c in -fe: A comparison between atomic simulations and elasticity theory. *Acta Materialia*, 56(14):3450–3460, August 2008.
- [46] C.S. Becquart, J.M. Raulot, G. Bencteux, C. Domain, M. Perez, S. Garruchet, and H. Nguyen. Atomistic modeling of an fe system with a small concentration of c. *Computational Materials Science*, 40(1):119–129, July 2007.
- [47] Y. Hanlunmyuang, P.A. Gordon, T. Neeraj, and D.C. Chrzan. Interactions between carbon solutes and dislocations in bcc iron. *Acta Materialia*, 58(16):5481–5490, September 2010.
- [48] W.A Spitzig and A.S Keh. Orientation dependence of the strain-rate sensitivity and thermally activated flow in iron single crystals. *Acta Metallurgica*, 18(9):1021–1033, Sep 1970.
- [49] Laurent Proville, David Rodney, and Mihai-Cosmin Marinica. Quantum effect on thermally activated glide of dislocations. 11(10):845–849.
- [50] Francesco Maresca, Daniele Dragoni, Gábor Csányi, Nicola Marzari, and William A. Curtin. Screw dislocation structure and mobility in body centered cubic Fe predicted by a Gaussian Approximation Potential. 4(1):69.
- [51] Graeme Henkelman, Andri Arnaldsson, and Hannes Jónsson. Theoretical calculations of CH<sub>4</sub> and H<sub>2</sub> associative desorption from Ni(111): Could subsurface hydrogen play an important role? 124(4):044706.
- [52] Antoine Kraych, Emmanuel Clouet, Lucile Dezerald, Lisa Ventelon, François Willaime, and David Rodney. Non-glide effects and dislocation core fields in BCC metals. 5(1):1–8.
- [53] R. Gröger and V. Vitek. Explanation of the discrepancy between the measured and atomistically calculated yield stresses in body-centred cubic metals. 87(2):113–120.
- [54] Graeme Henkelman, Blas P. Uberuaga, and Hannes Jónsson. A climbing image nudged elastic band method for finding saddle points and minimum energy paths. 113(22):9901–9904.
- [55] D. Caillard. Kinetics of dislocations in pure Fe. Part I. In situ straining experiments at room temperature. 58(9):3493–3503.
- [56] D. E. Jiang and Emily A. Carter. Carbon dissolution and diffusion in ferrite and austenite from first principles. 67(21):214103.
- [57] J.R.G. da Silva and Rex B. McLellan. Diffusion of carbon and nitrogen in B.C.C. iron. 26(1):83–87.

- [58] A. Ramasubramaniam, M. Itakura, M. Ortiz, and E.A. Carter. Effect of atomic scale plasticity on hydrogen diffusion in iron: Quantum mechanically informed and on-the-fly kinetic Monte Carlo simulations. *23*(10):2757–2773.
- [59] Ivaylo H. Katzarov, Dimitar L. Pashov, and Anthony T. Paxton. Hydrogen embrittlement I. Analysis of hydrogen-enhanced localized plasticity: Effect of hydrogen on the velocity of screw dislocations in  $\alpha$ -Fe. *1*(3):033602.
- [60] Yong Lu, Fawei Zheng, and Ping Zhang. First-principles study of temperature-dependent diffusion coefficients for helium in  $\alpha$ -Ti. *114*(15):153507.
- [61] B.J. Berne, G. Ciccotti, and D.F. Coker. *Classical and Quantum Dynamics in Condensed Phase Simulations: Proceedings of the International School of Physics*. World Scientific Publishing Company.
- [62] A Togo and I Tanaka. First principles phonon calculations in materials science. *Scr. Mater.*, 108:1–5, Nov 2015.
- [63] H. Yoshinaga and S. Morozumi. The solute atmosphere round a moving dislocation and its dragging stress. *23*(186):1367–1385.
- [64] Luis Casillas-Trujillo, Davide Gambino, Lisa Ventelon, and Björn Alling. Screw dislocation core structure in the paramagnetic state of bcc iron from first-principles calculations. *102*(9):094420.
- [65] B Lüthi, F Berthier, L Ventelon, B Legrand, D Rodney, and F Willaime. Ab initio thermodynamics of carbon segregation on dislocation cores in bcc iron. *Modelling and Simulation in Materials Science and Engineering*, 27(7):074002, July 2019.
- [66] P. Maugis and D. Kandaskalov. Revisiting the pressure effect on carbon migration in iron. *Materials Letters*, 270:127725, July 2020.
- [67] Wei Cai, Vasily V. Bulatov, Jinpeng Chang, Ju Li, and Sidney Yip. Periodic image effects in dislocation modelling. *Philosophical Magazine*, 83(5):539–567, January 2003.